Part I

Semiconducting Materials and Nanometer-scale Structures

Chapter 4

Nonequilibrium Structural Dynamics: Gallium Arsenide as a Prototype System[†]

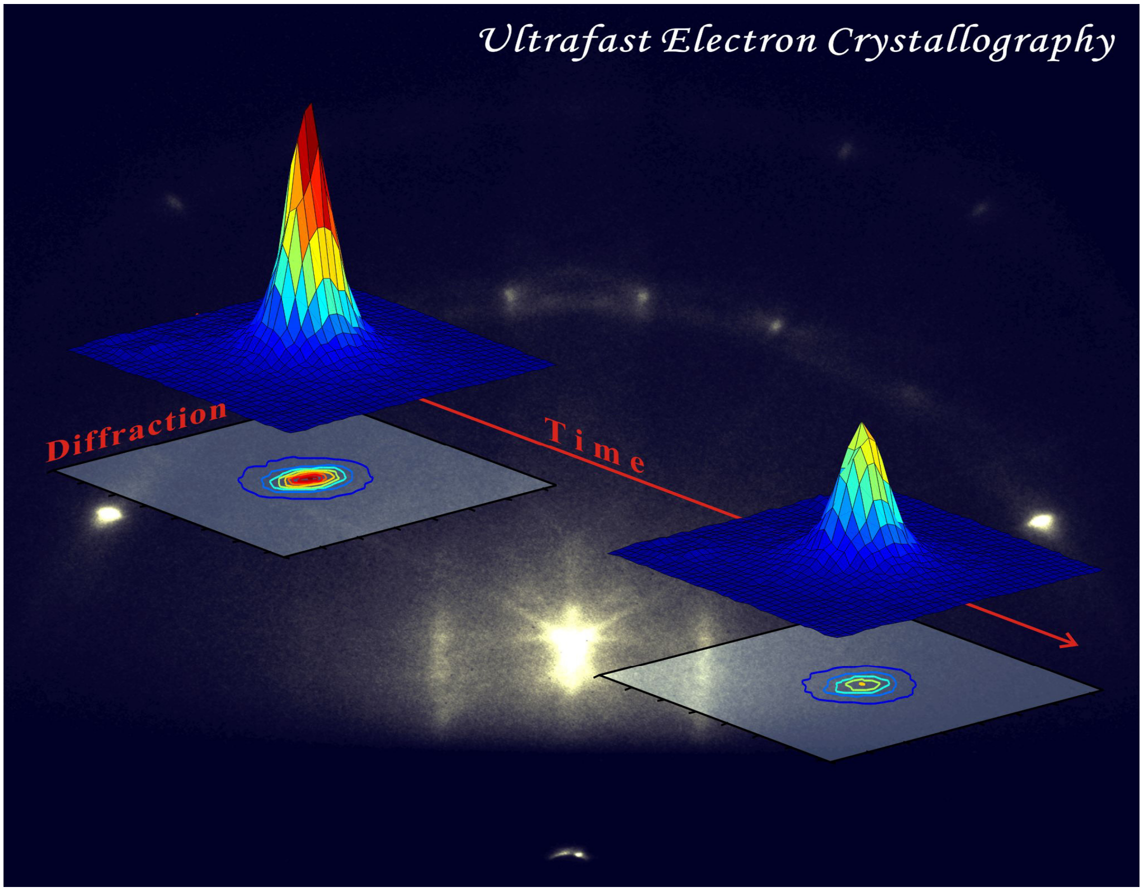

[†] adapted from D.-S. Yang, N. Gedik, A. H. Zewail, *J. Phys. Chem. C* **111**, 4889 (2007).

Introduction

In our laboratory, ultrafast electron diffraction and imaging have been developed to investigate structural dynamics with atomic-scale resolutions (*1, 2*). When it comes to the study of solid-state surfaces and nanometer-scale materials, the advantages of using electrons to probe the transient structures are evident. Because of the much higher electron–matter interaction cross section (small penetration depth) and the high sensitivity to structural changes, electrons are especially suitable for interfacial studies. Ultrafast electron crystallography (UEC) has been the method of choice for studies of such interfacial phenomena in different systems, including surfaces and phase transitions (*3, 4*), interfacial water (*5*) and self-assembled surface monolayers (Ch. 11), and biological model bilayers (*6-8*). For all of these studies, a clear understanding of the dynamics of the underlying crystalline substrate is critical to the characterization of the initial "temperature jump" and subsequent dynamics at interfaces.

Studies of substrates, such as silicon (*3, 6*), gallium arsenide (*4*), and gold (Ch. 11), have shown a universal behavior in that the observed transient, following a femtosecond excitation, displays a downward movement of Bragg diffraction spots (corresponding to increase in lattice interplanar spacings), decrease in total intensity and increase in diffraction width, all of which occur on the ultrashort time scale, from ~10 ps to ~100 ps depending on the system. At longer times, these changes reverse and the diffraction spots ultimately recover the original coordinates, certainly on the time scale between pulses, a millisecond in UEC.

Questions remained as to what causes these universal features and what are the actual nonequilibrium temperatures of the carriers and lattice. In this chapter, I present studies of the direct-gap semiconductor GaAs as a prototype system with a well-defined quantum-well structure of 20 nm thickness and "tuned" band gap energy. Comparisons with the results of the bulk material that has also been studied elucidate mechanisms of structural dynamics. Besides the obvious technological relevance, these semiconductor structures can be made to have atomically flat surfaces, their surface dangling bonds are unique in orienting adsorbates, and extensive studies of their optical responses using ultrafast spectroscopy have been made (*9, 10*). Both direct-gap (GaAs) and indirect-gap (Si) semiconductors are considered in our discussion of the dynamics, but the focus here is on the former. The discussion is extended to include the most significant properties that in general determine the structural dynamics of crystalline semiconductors.

This chapter combines the aforementioned experimental studies to provide a full account of the methodology and its potential in different applications. Sample preparation and the two UEC detection modes, reflection and transmission, are described. Results and analysis are presented for studies made at different excitation wavelengths and detection modes. The Discussion Section covers the key processes involved with carrier excitation, and the lattice motions that cause changes in diffraction features on the short and long time scales. Lastly, a physical picture of structural dynamics is provided to conclude the current investigation.

Materials and Experimental Section

For the transmission experiments, thin GaAs films of 20 nm thickness supported on empty gold grids (Ted Pella, Inc., 300 mesh), or on the grids that have carbon-based support films (Ted Pella, Inc., #01810G-F), were prepared following the procedure reported by Konkar *et al.* (*11*). The lattice-matched heterostructure consisting of a 20-nm GaAs layer above a 50-nm $Al_{0.6}Ga_{0.4}As$ layer was grown on a 450-μm GaAs(001)

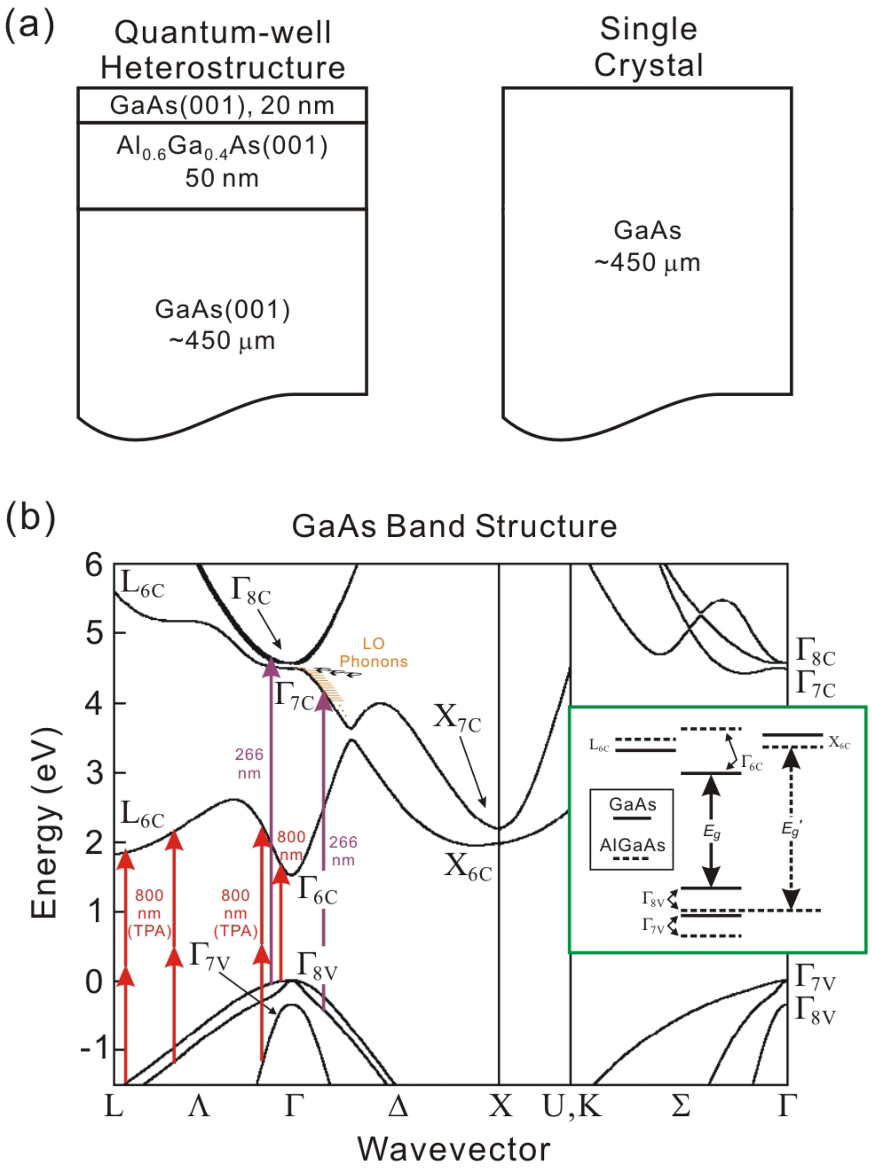

Fig. 1. Crystal and band structure. (a) Comparison of the quantum-well heterostructure studied and the single crystal used in Ref. 4. (b) The electronic band structure of GaAs (*12*) is shown, and the excitations at two different wavelengths (266 and 800 nm) are indicated. Carriers are initially prepared in different regions of the band structure, and their energy relaxation proceeds through optical-phonon emission; the orange short lines indicate different electronic states (Bloch functions) with different crystal wavevectors. The inset shows the band energies at three high-symmetry points (Γ, L and X) for GaAs (solid lines) and $Al_{0.6}Ga_{0.4}As$ (dash lines) (*13*). The direct band gap of GaAs (E_g) and indirect band gap of $Al_{0.6}Ga_{0.4}As$ (E_g') are also indicated.

substrate (Fig. 1a) using the molecular-beam epitaxy (MBE) method (MBE lab at University of California, Santa Barbara). The band structure of GaAs (*12*) and the energetics for the carrier excitation processes are displayed in Fig. 1b; the inset presents a comparison of the band energies at three high-symmetry points for GaAs and $Al_{0.6}Ga_{0.4}As$ (*13*). After the successive mechanical polishing and chemical etching procedures, 20-nm GaAs thin films covered an area of up to ~1 mm^2 on the gold grids. Inside the diffraction chamber, the whole sample area was illuminated by the excitation pump beam, while the electron probe beam was at the central part of the laser-heated region. The $[1\bar{1}0]$ axis of the thin film was oriented vertically (in the laboratory coordinate system) and became the rotational axis. By rotating the GaAs film, we were able to access different crystal planes other than (001). Samples on a grid with or without the carbon-supported film showed the same diffraction patterns.

For the reflection experiments, the heterostructure samples were cleaned by dipping them into a concentrated HCl solution for a few seconds, followed by a fast rinse by deionized water, to remove any native surface oxide. It is known that this cleaning process may increase the amount of elemental arsenic with residual chlorine species on top of the GaAs surface (*14*). From our experiments, no significant effect on structural dynamics from this surface “contamination” was seen. The finite penetration of electrons guaranteed that only the lattice of the GaAs quantum well was probed even if a Bragg spot of relatively higher order (i.e., a relatively large incidence angle) was under investigation to reduce any surface or refraction effect.

The original excitation scheme was used for the current study. The initiating pulses were directed and loosely focused (area of illumination ~ 1.66 mm^2) at an incidence angle of ~60° from the substrate surface normal, to initiate the “temperature

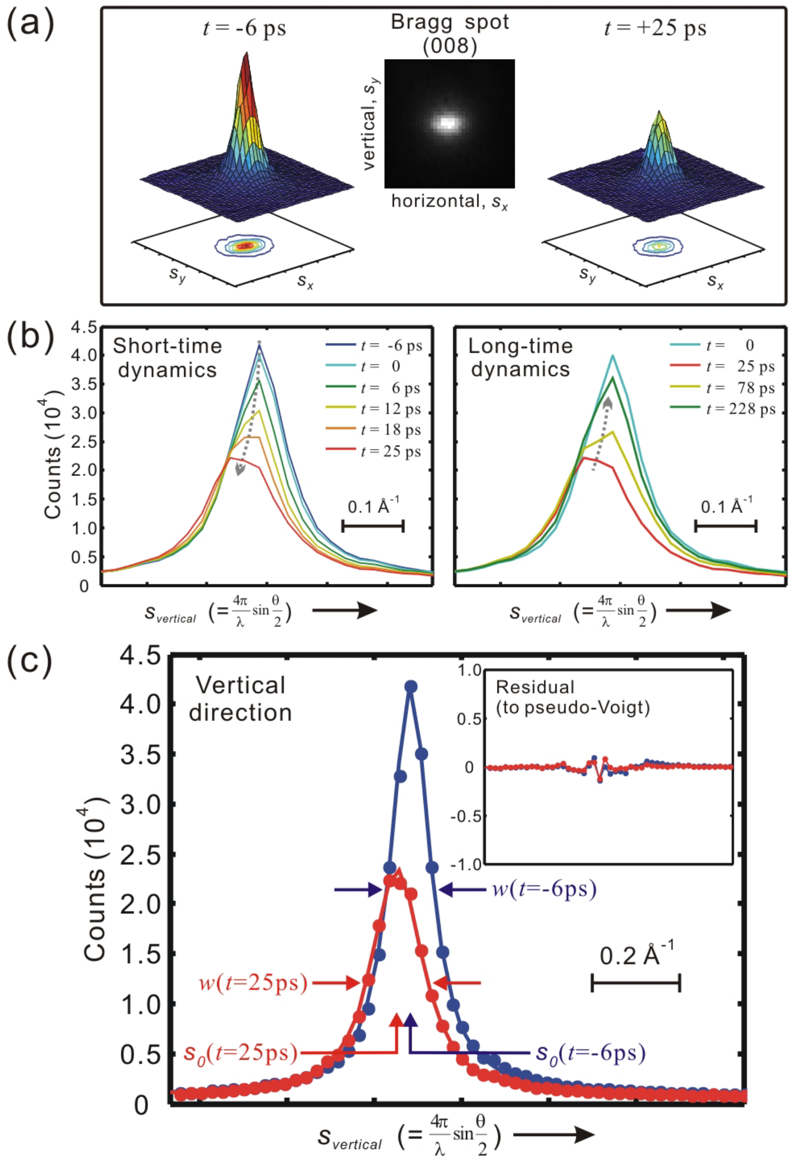

Fig. 2. Bragg spot (008) temporal change. (a) 3D profile and its contour plot of the diffraction at two times, –6 and +25 ps. (b) Left: Short-time dynamics. The initial change is a decrease of the Bragg intensity with little spot movement (0–12 ps), followed by a clear peak shift with more intensity depletion (12–25 ps). Right: Long-time restructuring dynamics. After the minimum spot intensity and maximum position shift are reached, the diffraction profile undergoes a recovery toward the equilibrium state. (c) Fitting of the vertical diffraction profile at $t = -6$ and 25 ps, with the peak position (s_0) and the fwhm (w) indicated for each case. The results of fitting (lines) match very well with the acquired data (dots), and the residuals are shown in the inset. The apparent width gives the minimum coherence length as the total width has a contribution from the instrument function.

jump.” In order to minimize the temporal mismatch between the optical and electron pulses and eliminate the interference of diffraction from the unexcited area, a rectangular specimen was oriented so that only a small corner region would be probed. In this way, changes after 1-ps delay could be observed while the number of electrons per pulse was ~2000. The electron beam traveled along the [010] direction (with a grazing incidence angle), and the polarization of the heating pulses was along the $[1\sqrt{3}0]$ direction. From the angular separations between spots on side streaks and the lattice constant of GaAs ($a = 5.653$ Å), a camera length of 16.90±0.03 mm from the scattering position was deduced. The angular difference and scattering-vector change between high-order Bragg spots (0 0 4*n*) on the central streak also confirmed the correctness of the calculated camera length and the (001) crystal-surface orientation (see Ch. 2). In the reflection experiments, we focused on the dynamics of the (008) Bragg spot (Fig. 2a).

Results and Analysis

The diffraction patterns recorded for the equilibrium structure at room temperature serve as the negative-time frame reference because they represent the system in its thermodynamic equilibrium. At a given delay time, we then obtain the change in diffraction, and with the frame-reference method, the sensitivity is as low as 1% for UED (*2*) and 0.02% for UEC (because of the collective change). In the reflection experiments, the difference images almost always show, around the diffraction spots or rings, an intensity reduction at the original locations and enhancement in the neighboring regions closer to the direct beam position at positive times, which means that the Bragg reflections are shifted toward the smaller *s* values (Fig. 2b, left panel). This is the signature of lattice expansion following the optical excitation, a direct conclusion from the Laue condition discussed in Ch. 2. If the fluence of the initiating pulses is increased, stronger reduction of the intensities may be seen prior to the emergence of enhancement in the neighboring regions (Fig. 2b, left panel), indicating that certain lattice motions, which cause the Bragg intensities to decrease, occur prior to any appreciable lattice expansion. In this geometry, the observed result was always the change of the diffraction images along $\hat{n}$ without a clear horizontal movement of the Bragg spots (within our experimental temporal range), which is a signature of an anisotropic change in the crystalline structure at short times. Different materials show the maximum reduction of intensities and movement of positions at different delay times, and recovery of those changes (Fig. 2b, right panel) is universal even though their rates may differ.

It should be noted that the observed downward shift of Bragg diffraction reflects the genuine lattice expansion following the optical excitation, and does not result from a downward shift of the direct electron beam trajectory at positive times. To confirm this conclusion, we have simultaneously recorded, by removing the electron beam trap, diffraction patterns together with the direct electron beam projection on the camera. It was observed that, whereas the Bragg spots of the lattice were clearly shifting downward, at early times, the direct beam position made very little of a change and even moved slightly upward. Such an observation, together with the parallel Bragg intensity change at short times, excludes the possibility of an artifact caused by electron-beam shifting due to electronic excitation of the substrate surface.

In the transmission study of a crystalline thin film, by subtracting the negative-time reference frame from the diffraction images, reduction of spot intensities at the spots' original locations can be seen at a positive time after the heating pulse excites the sample, but the recovery is very slow within our temporal window. Another

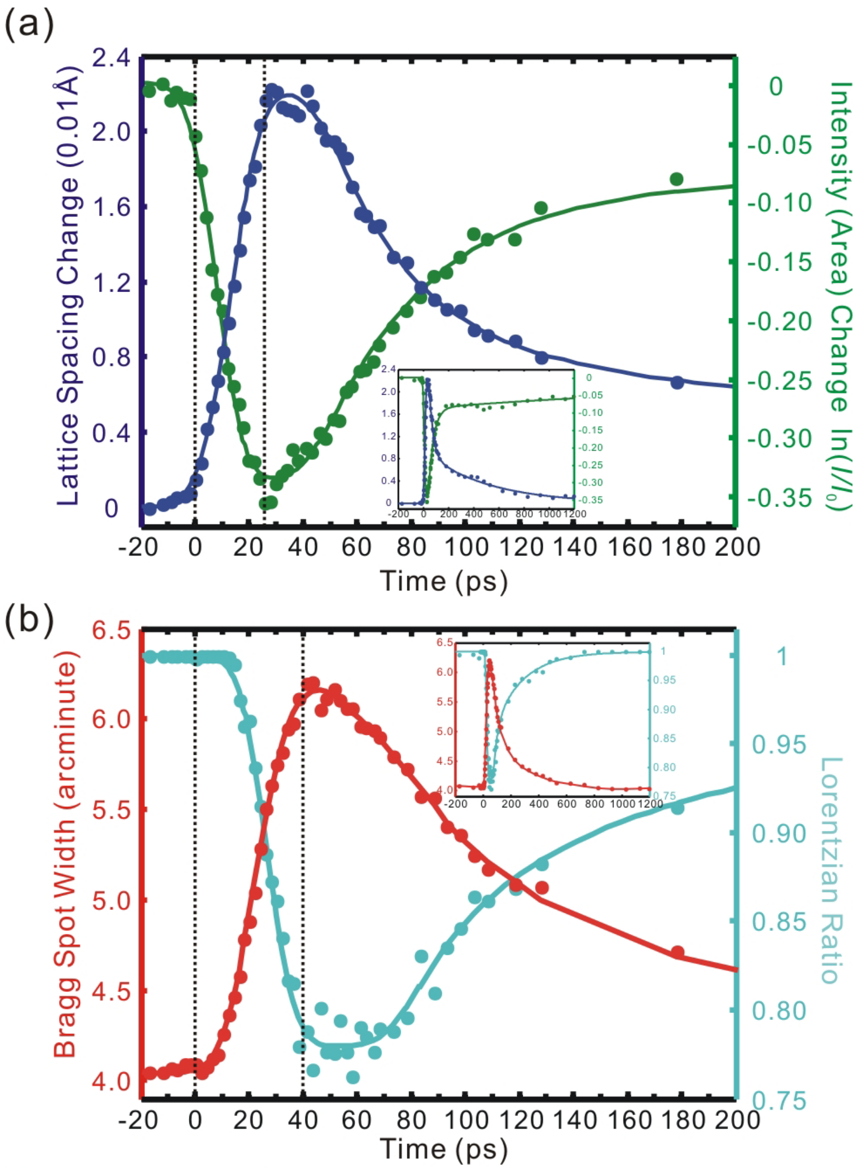

Fig. 3. UEC experimental observations made at 266-nm excitation, fluence 2.2 mJ/cm^2. (a) Early-time behavior of changes in the (008) spot intensity, ln[$I(t)/I_0$] (green dots), and lattice spacing, $\Delta d_{001}(t)$ (blue dots); the solids lines (and also those in the following figures) are made to guide the eyes unless specified. The maximum changes can be observed at $t = 25$ ps as indicated by the dash line. The long-time behavior of temporal changes is shown in the inset. Note the residual changes at $t = 1.2$ ns. (b) Early-time behavior of changes in the (008) spot width, $w(t)$ (red dots), and Lorentzian component, $\eta(t)$ (cyan dots). The maximum changes are seen at a later time, $t = 40$ ps. The long-time behavior is shown in the inset; the two curves return to their negative-time equilibrium values before $t = 800$ ps.

interesting observation is that, unlike the reflection counterpart, the spot positions do not exhibit a substantial movement during the entire temporal range, which leads us to the conclusion that in-plane lattice expansion is negligible. The lack of horizontal shifts for Bragg spots in the reflection detection and in-plane spot movements in the transmission detection points to a consistent physical picture of the vertical (relative to the surface normal) structural changes at short times as being the major contribution to dynamics; see Ch. 2 for the theoretical discussion.

Quantitative analysis of the observed diffraction transient changes was made for the present study of the GaAs(001) heterostructure and thin film, by using the fitting procedure described in Sec. B.5 of Ch. 2. In what follows, I represents the (1D) integrated intensity, s the scattering vector, s_0 the peak position of the Bragg spot, w the full width at half maximum (fwhm), and η the Lorentzian contribution. Because the surface quality was good enough to reduce inelastic and other scattering events, only flat and very low background intensity was seen and no background subtraction prior to fitting was needed; see Fig. 2c for two examples of the fitting results. Comparisons between the extracted diffraction features—$I(t)$, $s(t)$, $w(t)$, and $\eta(t)$, where t is the delay time between the electron and optical pulses—and between the results at different excitation fluences and wavelengths, and in different detection modes, were made to elucidate the structural dynamics and relaxation pathway in GaAs.

A. Reflection Experiments

Figure 3 shows the temporal change of the integrated intensity $I(t)$, lattice constant change $\Delta d_{001}(t)$ along $\hat{n}$ [derived from $s(t)$ using $\Delta d_{001}(t) / a = -\Delta s(t) / s_0(t<0)$], vertical spot fwhm $w(t)$ and the ratio of the Lorentzian component $\eta(t)$ extracted from the vertical fitting of the (008) Bragg spot; all recorded in the reflection experiment with an

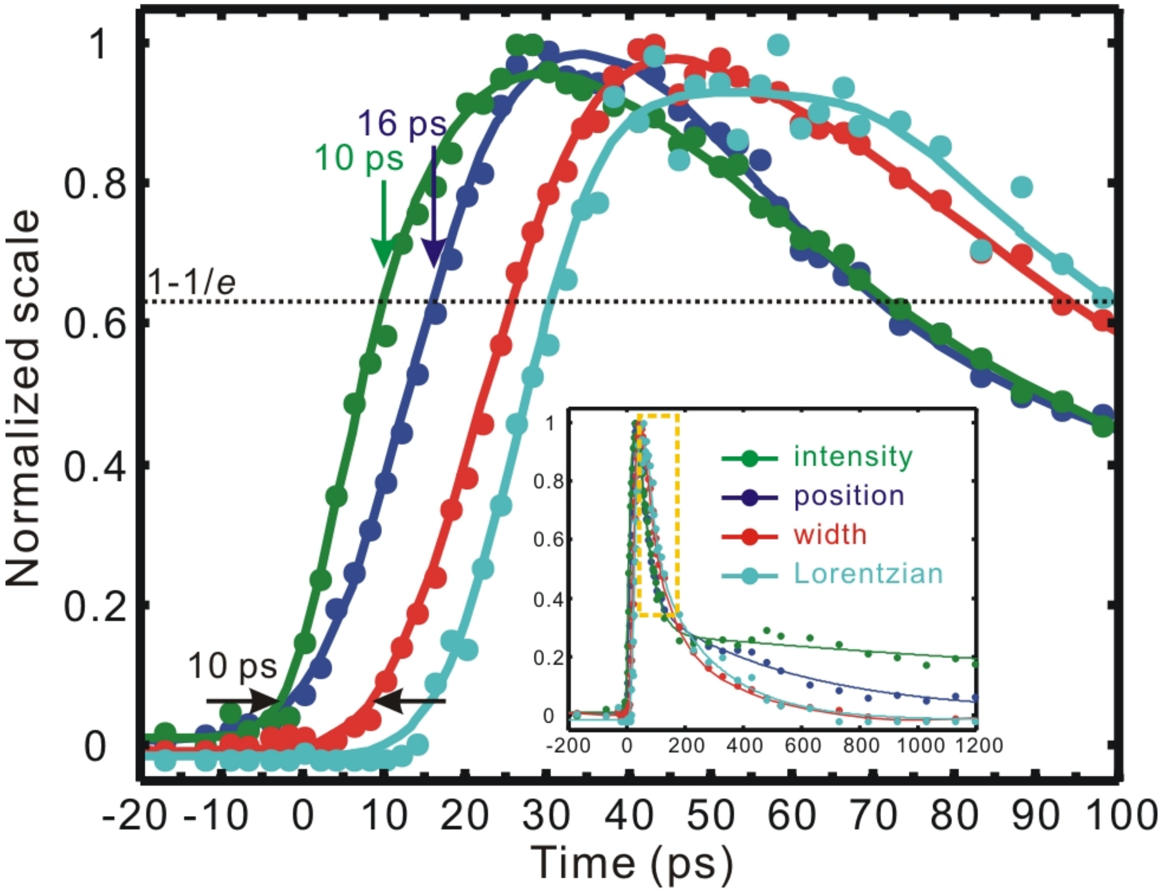

Fig. 4. Ultrafast prompt and delayed diffraction features. Comparison of the early-time behavior of $I(t)$, $\Delta d_{001}(t)$, $w(t)$, and $\eta(t)$ of the (008) Bragg spot is shown on a normalized scale. Clearly, the changes of the width and Lorentzian component are delayed from those of the intensity and lattice spacing by 10 ps (or more). If an exponential rise function is considered, the $1 - 1/e$ value (dash line) in the temporal curves gives the rise times of intensity and lattice spacing change to be 10 and 16 ps, respectively. The inset shows the long-time behavior; $w(t)$ and $\eta(t)$ are similar over the whole temporal range, while a larger residual change is observed in $I(t)$ than in $\Delta d_{001}(t)$ at $t = 1.2$ ns. Within the yellow dashed box, the four profiles are seen to closely resemble each other.

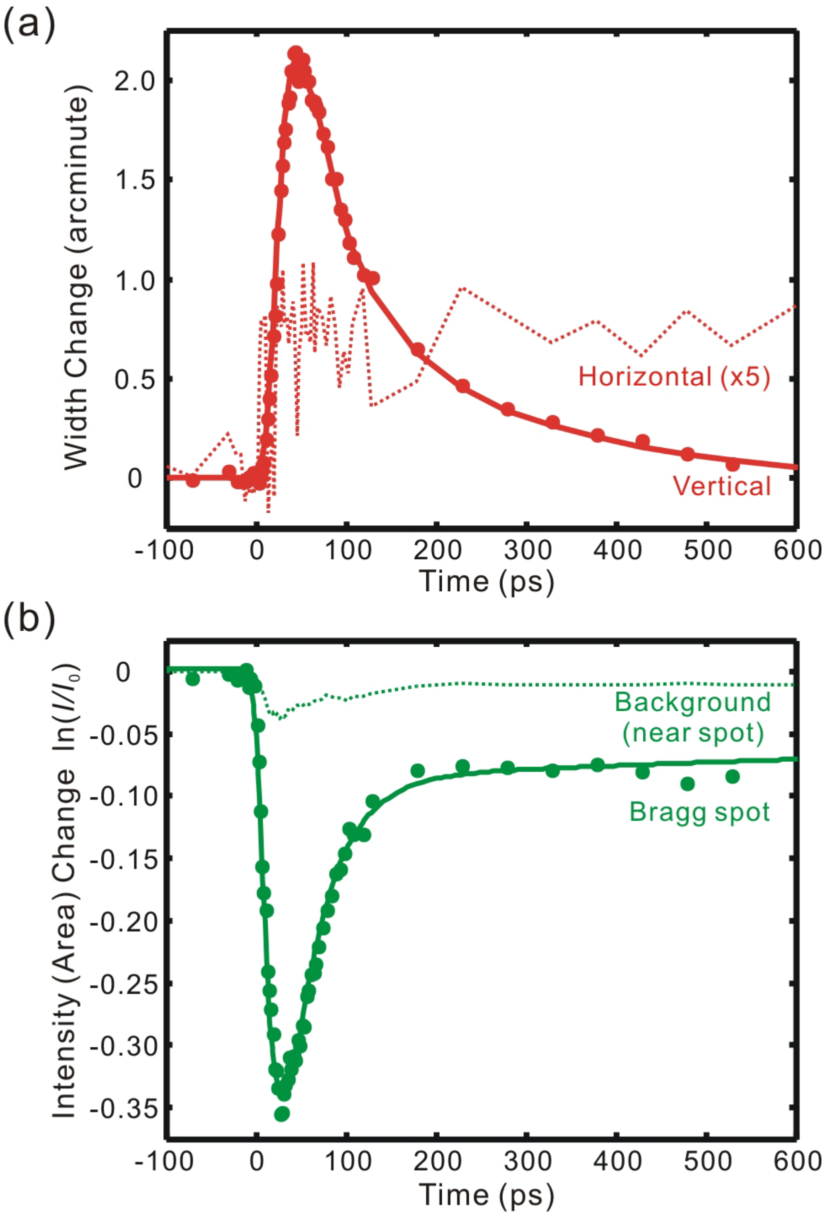

Fig. 5. Diffraction width anisotropy and background scattering. (a) Vertical and horizontal width changes of the (008) Bragg spot as a function of time. Compared to the smooth temporal behavior (rise and decay) of large vertical width change, the horizontal width changes insignificantly and remains for hundreds of picoseconds. (b) Intensity change of the Bragg spot and that of the background in the spot's vicinity. The large amplitude difference shows that the intensity reduction is not due to an overall intensity change of the diffraction pattern.

excitation fluence of 2.2 mJ/cm^2 at 266 nm. At first glance, the four curves seem to exhibit a similar temporal behavior: no change at negative time, rapid change within the first ten(s) of picoseconds immediately after the initiation at the zero of time (t_0), fast recovery on a time scale of tens of picoseconds after the peak change is reached, and finally slower recovery toward the equilibrium structure on a sub-nanosecond to nanosecond (and longer) time scale. However, careful examination brings about several important observations in the temporal behavior of the different diffraction features.

First, the rise part of $\Delta d_{001}(t)$ and $I(t)$ develops and reaches the extremum at $t = 25$ ps with a time constant $\tau \sim 10$ ps (Fig. 3a). This implies that the time scale for the vertical lattice expansion and structural change is ultrafast. Second, the increase in the changes of $w(t)$ and $\eta(t)$ is clearly delayed by ~10 ps behind those of $I(t)$ and $\Delta d_{001}(t)$ (Fig. 4), indicating that dynamical inhomogeneity occurs with a delay or “threshold” in time; the same phenomenon was also confirmed in the dynamics of the (0 0 12) Bragg spot. Third, the change of $I(t)$ grows faster than that of $\Delta d_{001}(t)$, within the first 25 ps, as shown in Fig. 4; the time for $I(t)$ to reach $1 - 1/e$ of its maximum change is apparently smaller than that for $\Delta d_{001}(t)$. Fourth, the horizontal width change as a function of time shows only a positive plateau reached at early time without any noticeable recovery on our time scale, and the amplitude is less than 1/10 of the maximum vertical width increase (Fig. 5a). This difference is a manifestation of the anisotropy in the transient structural change, as discussed above. To further confirm that the background scattering has no effect on the dynamics, we checked the temporal behavior of the background intensity in a rectangular area in the vicinity of the (008) Bragg spot. As shown in Fig. 5b such a contribution, if any, is negligible.

For the other excitation at 800 nm (fluence of 10.9 mJ/cm^2), the temporal change

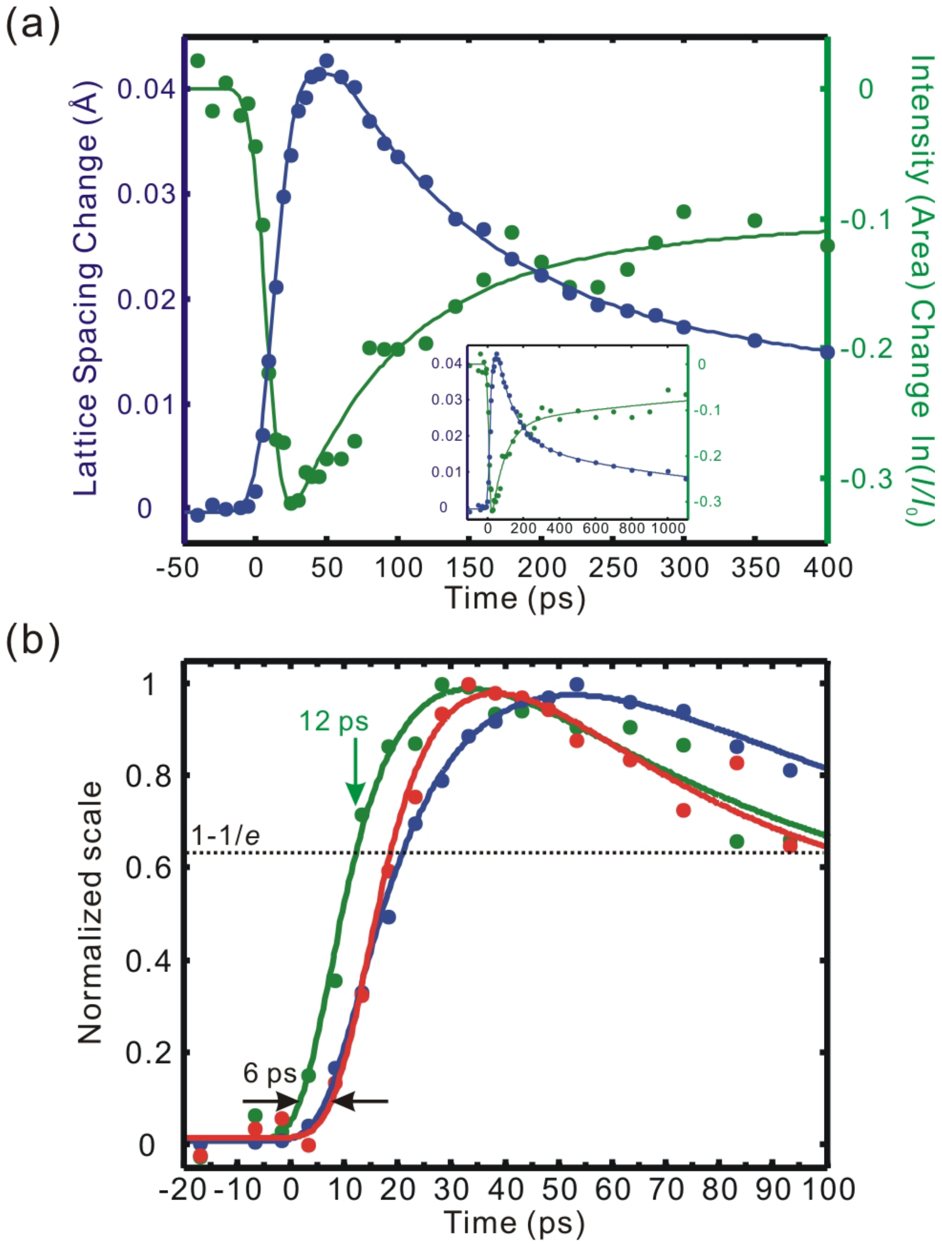

Fig. 6. UEC experimental observations made at 800 nm, fluence 10.9 mJ/cm^2. (a) Early-time behavior of changes of the (008) spot intensity, ln[$I(t)/I_0$] (green dots), and lattice spacing, $\Delta d_{001}(t)$ (blue dots). The long-time behavior is shown in the inset. (b) Comparison of the early-time behavior of $I(t)$, $\Delta d_{001}(t)$, and $w(t)$ of the (008) Bragg spot on a normalized scale. Again, $w(t)$ (red dots) is delayed by 6 ps from $I(t)$, but the two curves share a similar rise time of 12 ps. After the maximum changes are reached, the three diffraction features recover with a similar decay rate.

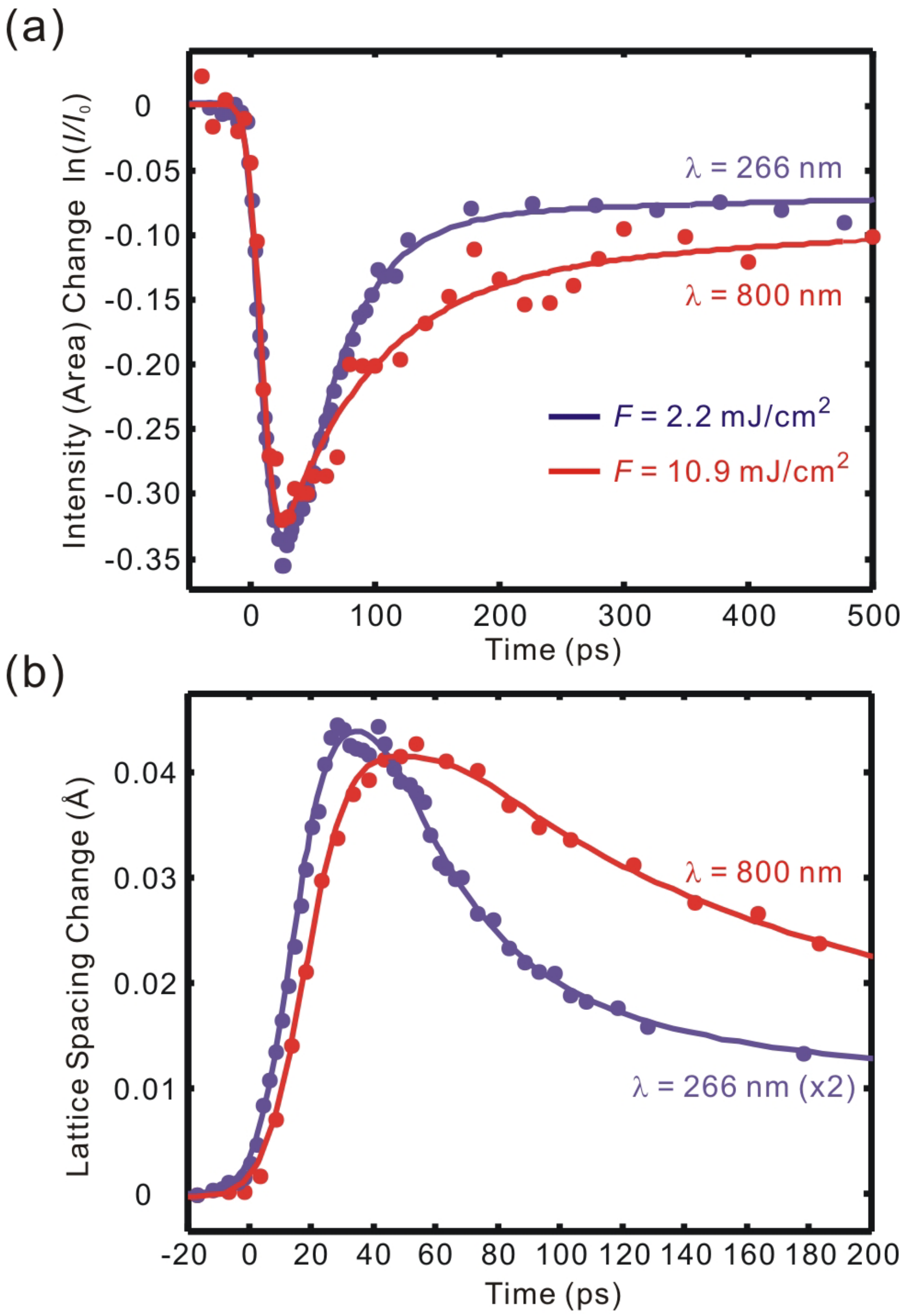

Fig. 7. Effect of fluence and initial excitation. (a) Comparison of (008) spot intensity change; (b) lattice spacing change at the two wavelengths, 266 nm (blue dots) and 800 nm (red dots). Similar profiles for the rise of intensity reduction are observed, with the maximum change occurring at $t = 25$ ps. Lattice expansion at 800 nm is about twice as large as that at 266 nm, although the former one rises more slowly than the latter (see Text for discussions in detail).

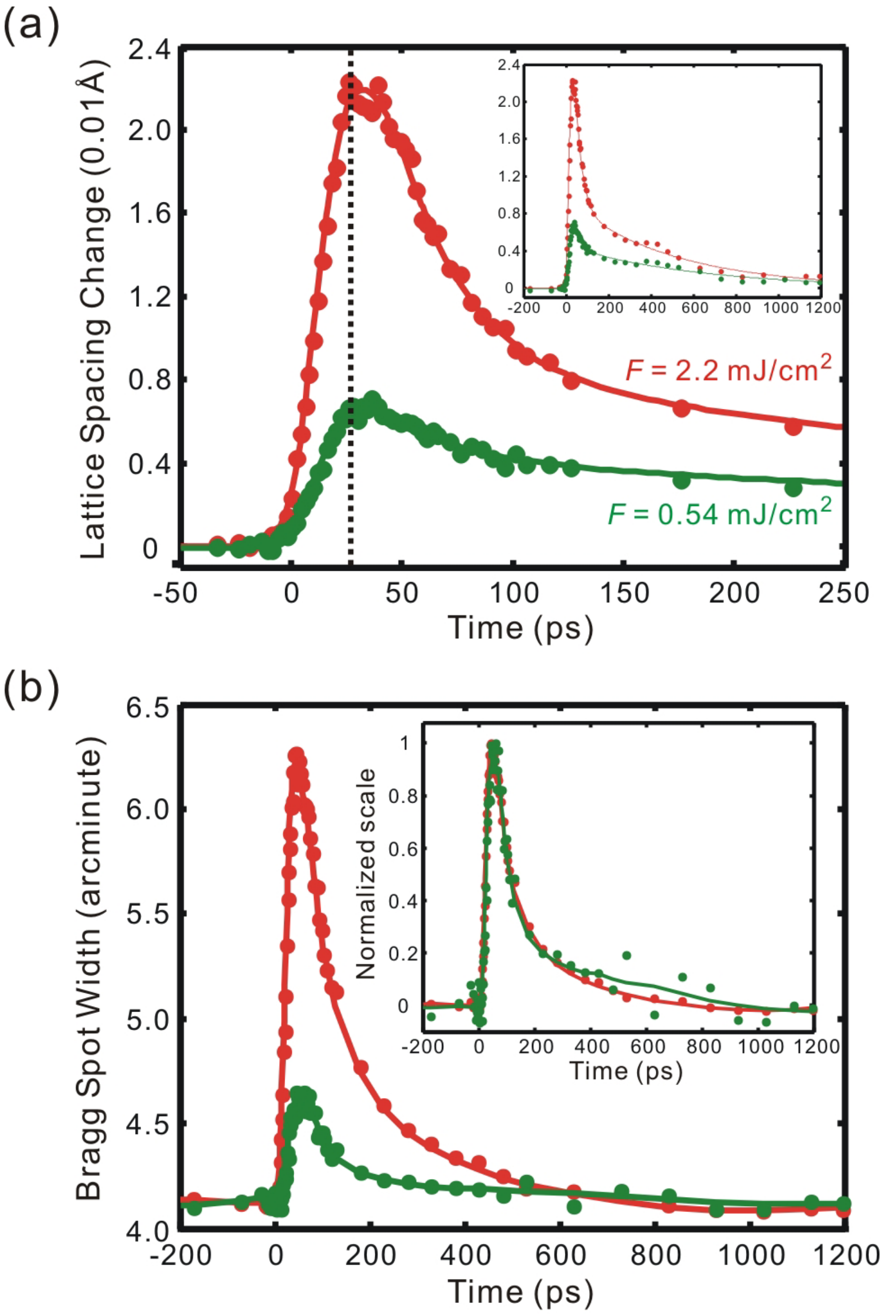

Fig. 8. Fluence dependence at 266 nm. (a) The maximum lattice expansion is observed at $t = 25$ ps regardless of the excitation fluence used, suggesting the same rise time for both cases. The inset shows the long-time behavior and the faster recovery in the high-fluence case. (b) The maximum vertical width change is seen to be linear with the excitation fluence, and the temporal behavior remains essentially unchanged, as shown on a normalized scale in the inset.

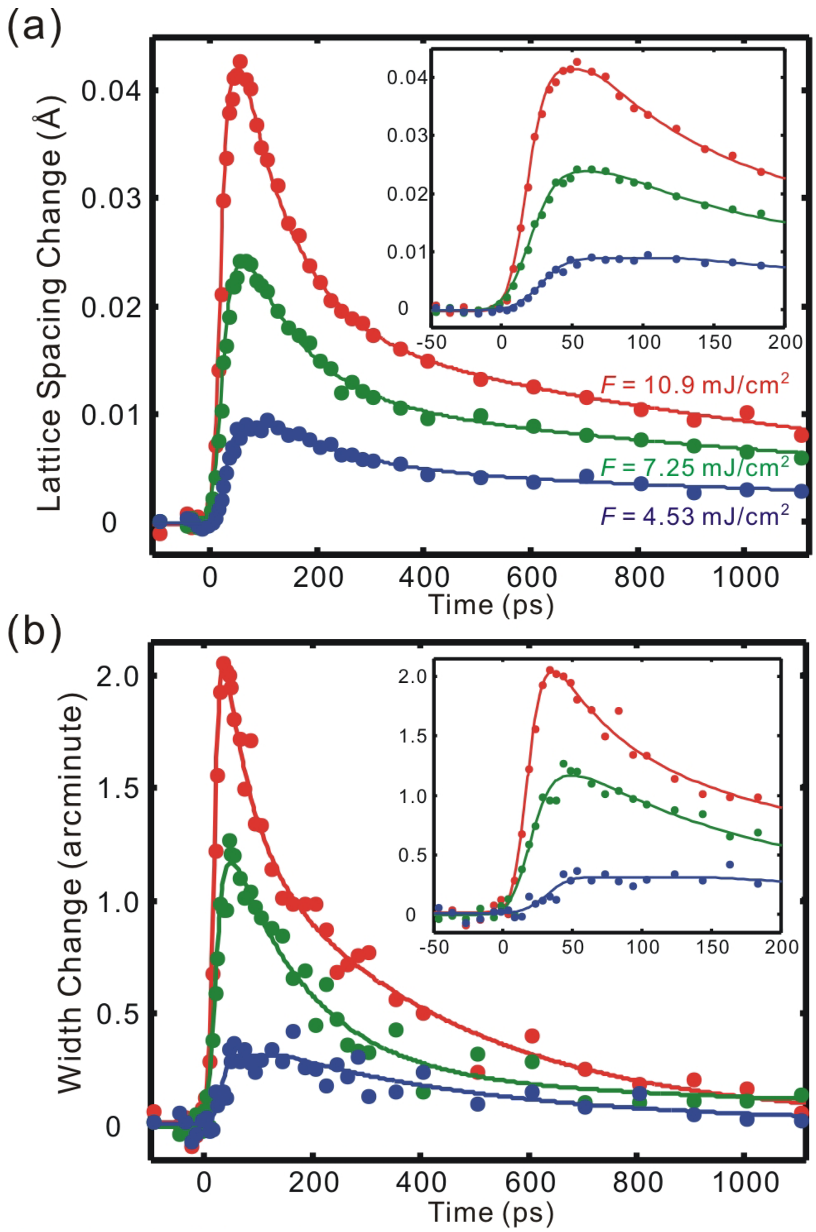

Fig. 9. Fluence dependence at 800 nm. (a) Long-time behavior of the lattice spacing change at three different fluences, with the early time shown in the inset. The maximum expansion is not linear with the fluence due to the two-photon excitation phenomenon. Faster recovery can be observed at high excitation fluences. (b) Similar fluence dependence is seen for the width change: the higher the fluence, the larger the initial fast recovery. In contrast to the results of Fig. 7b, these curves do not resemble each other after normalization.

of the (008) Bragg spot, $I(t)$ and $\Delta d_{001}(t)$, shows similar behavior: a fast rise at early time followed by a seemingly two-component recovery in 1 ns (Fig. 6a). If we plot $I(t)$, $\Delta d_{001}(t)$, and $w(t)$ on a normalized scale, as shown in Fig. 6b, and zoom into the initial changes, it is found that the rise part of $I(t)$ again is not instantaneous but reaches the extremum at $t = 25$ ps; the initial development of the change seems to be very similar at two different excitation wavelengths (Fig. 7a). The increase of the change of $w(t)$ is clearly delayed by ~6 ps behind that of $I(t)$, a phenomenon that is also seen in the previous case of 266-nm excitation. However, the rise part of $\Delta d_{001}(t)$, instead of following closely with that of $I(t)$, is also delayed (Fig. 6b) and has an even slower growth to reach the maximum (Fig. 7b). Such a temporal difference in the behavior of $\Delta d_{001}(t)$ with respect to that of $I(t)$ at two different excitation wavelengths indicates a difference in the dynamics of lattice expansion. It is noticed that the maximum changes of $I(t)$ and $\Delta d_{001}(t)$ are similar or of the same order of magnitude (Fig. 7), suggesting that the lattice receives a similar amount of energy from the photoinjected carriers at early time.

Figures 8 and 9 present the results of the fluence-dependent studies at the two excitation wavelengths. The most noticeable change in the pattern of the dynamics is that, as the excitation fluence at 800 nm is decreased, the prominent peaks of the change of $I(t)$, $\Delta d_{001}(t)$, and $w(t)$ at early times are greatly diminished, and both rise and decay time scales appear to be slower. In contrast, the results from the 266-nm experiments do not show such a pattern change; in fact, after normalization, $w(t)$ is essentially independent of the fluence (Fig. 8b, inset). As will be shown in the Discussion Section, the fluence dependence at 800 nm is the manifestation of a two-photon carrier excitation reaching a different state due to the dispersion of the electronic band structure.

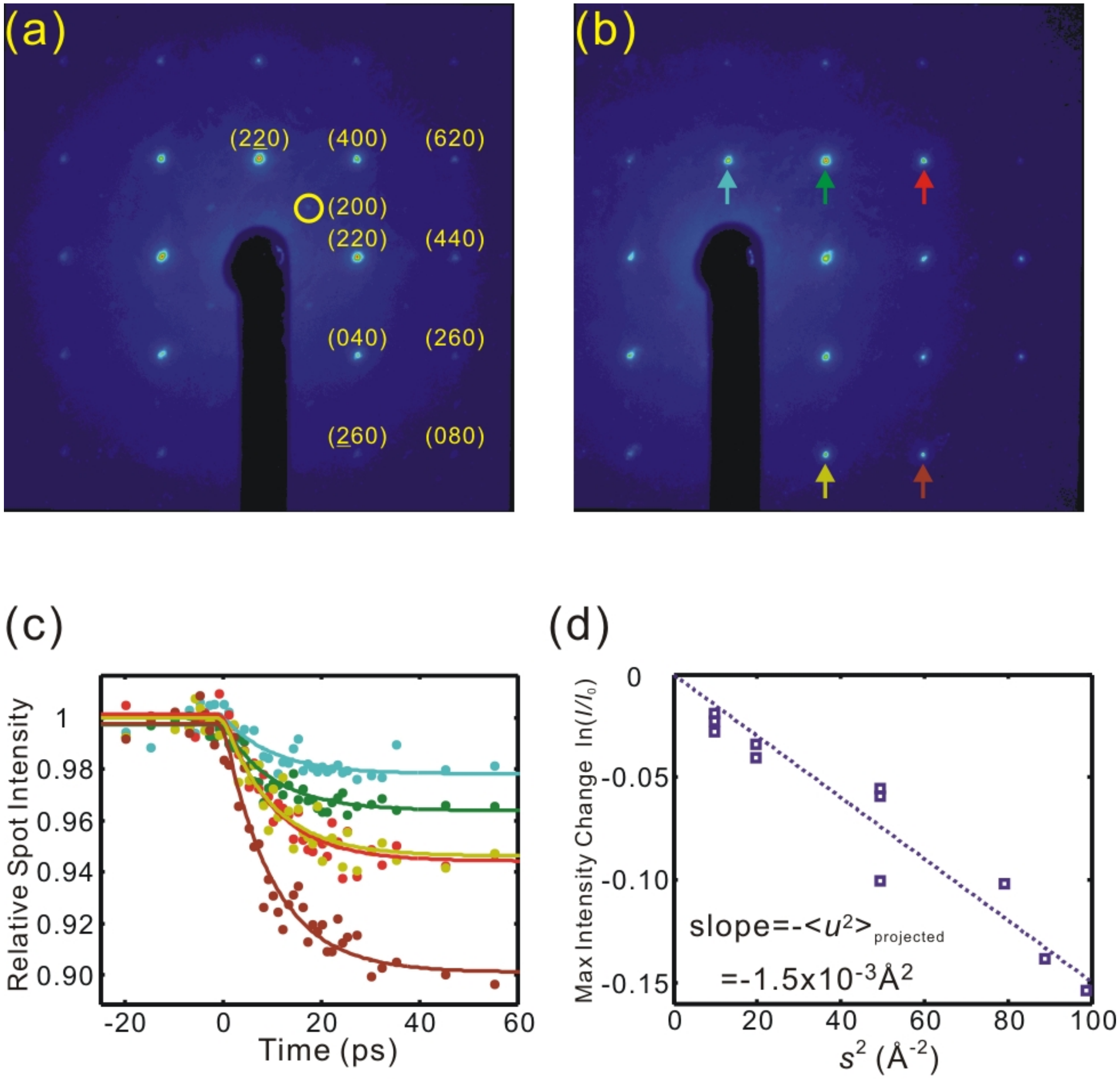

(See next page for the figure caption.)

Fig. 10. (a) Transmission diffraction pattern of GaAs(001). Electrons propagate along the surface normal direction; the black region is the projection of the electron-beam trap on the camera. Miller indices for several Bragg spots are given. (b) Transmission pattern recorded when electrons propagate along a direction 2° away from the normal. The diffraction pattern becomes asymmetric and the Bragg spots on the right-hand side become more intense. Intensities of different spots (some of them are indicated by arrows with different colors) are monitored as a function of time, as shown in (c). Spots with higher Miller indices have larger intensity drops (brown dots), and those spots with the same s [e.g., the two indicated by the red and yellow arrows in (b)] share very similar temporal behavior (red and yellow dots). The intensity reduction curves are fitted by a function of exponential growth, and the same time constant of 10 ps is obtained (solid lines), as in reflection experiments. (d) The maximum intensity changes (on a log scale) is plotted as a function of s^2. A linear relationship is obtained, and the slope is directly related to the vertical atomic motions along $\hat{n}$ (see Text for discussions).

B. Transmission Experiments

A typical diffraction image of the GaAs thin film along the [001] axis is shown in Fig. 10a; the principal axes and Miller indices of some Bragg spots are labeled. By following the intensities of the Bragg spots through the measurement of rocking curves and calculating the corresponding angular spans, we obtained a vertical width of ~0.15 Å^{-1} for the reciprocal rods. With the use of the Scherrer formula (Eq. 23 of Ch. 2), the effective crystalline thickness is estimated to be similar to the known thickness of the GaAs layer, 20 nm.

The GaAs thin film was excited by 266-nm light. No systematic temporal change of the spacing between the spots or in the widths was observed. Figure 10b shows the diffraction image probed along an axis 2° away from the [001] direction, and the intensities of various spots acquired by fitting at different delay times are presented in Fig. 10c. It is found that those Bragg spots with the same amplitude of scattering vectors, for example, (400) and (040) spots, or (620), (260), and $(\bar{2}60)$ spots, have the same behavior (see Fig. 10c for one example). The small intensity change is noticed, as compared to a 30% intensity depletion observed by the reflection method. Different types of gold grids were used to check if the support film on the grid has an effect, but we failed to find major differences in the depletion of spot intensities.

The temporal evolution of all spot intensities can be fitted by a function of exponential growth (convoluted with a proper instrumental response time), and this gives a time constant of ~10 ps. This rise time is reminiscent of what is seen in the reflection experiments at 266 nm. However, instead of recovering from the depleted values, as in the reflection results, the low intensities were sustained for the rest of the temporal range probed. This is expected given the confinement of lattice energy within a thin film and the nature of energy dissipation in a bulk sample; neither does the support film on the gold grid facilitate fast recovery in the GaAs thin film. Finally, we note in Fig. 10c the linear correlation between maximum intensity change for different Bragg spots and the value of s^2 (Fig. 10d), a point that we shall return to in the Discussion Section.

Discussion

The significant observations of the diffraction changes made in these UEC studies can be summarized as follows. First, in reflection experiments, the main diffraction features, $I(t)$, $s(t)$, $w(t)$, and $\eta(t)$, develop their temporal changes on the ultrashort time scale (typically $\tau \sim 10$ ps) and recover toward the equilibrium-state values with multiple time constants, ranging from 30 ps to nanoseconds. In transmission, $I(t)$ also decreases with $\tau = 10$ ps, similar to the reflection case, except that the recovery is not observed within our temporal range. Second, although a seemingly similar behavior (development of change and recovery) is observed for $I(t)$, $s(t)$, $w(t)$, and $\eta(t)$, differences such as delay of the onset of change and rates of development and recovery, can be clearly seen and resolved with our temporal response. Third, the dynamics is strongly dependent on the excitation wavelength and fluence. Fourth, the anisotropy of changes of the spot position and width in the vertical and horizontal directions is evident. In what follows, we address the nature of the nonequilibrium dynamics derived from these UEC observations.

A. Thermal vs Carrier Excitation

A.1. Thermal Heating and the Two-temperature Model

According to the thermal excitation mechanism discussed in Sec. B.1 of Ch. 2, one would have expected, given the highest heating fluences of 266 and 800-nm light used in this study, the maximum lattice expansion at 266 nm to be more than 2 orders of magnitude larger than that at 800 nm. This would be expected because of the huge difference in the temperature rise ΔT_l, which results from the excess energy above the band gap (E_{excess}) and the penetration depth δ (see Eq. 34 of Ch. 2). Also, according to the Debye–Waller factor (Eq. 16 of Ch. 2), this difference in ΔT_l should lead to a pronounced intensity reduction at 266 nm and a negligible change at 800 nm. Furthermore, because of the nature of thermal equilibrium, the widths and shapes of Bragg spots would have to be the same without major temporal changes since the crystal on the average preserves its order (Sec. B.2 of Ch. 2); horizontal lattice expansion due to the temperature rise would have been expected, too. However, as seen from the results (particularly, Fig. 7), the experimental observations contradict the above predictions, and in fact, a reverse trend was observed, as shown in Fig. 7b; the maximum expansion at 800 nm was observed to be twice as large as that at 266 nm. In another experiment with a different incidence angle to record the dynamics of the (206) and $(\bar{2}06)$ Bragg spots on the side rods, no sign of horizontal movement in their positions throughout the entire temporal range was seen, indicating the absence of a horizontal lattice expansion. As a result, the thermal-heating picture fails to account for the structural dynamics on the time scale probed by UEC.

The application of the two-temperature model (*15, 16*) to describe the carrier and lattice dynamics also becomes invalid in the case of semiconductors. In metals, various spectroscopic results have been successfully explained by this model (see, e.g., Refs. 17 and 18 and cited references therein; for a review on the carrier and phonon dynamics in semiconductors, see Ref. 19). Because of the ultrafast equilibration within the electron subsystem on the time scale of a hundred femtoseconds, a temperature is assigned to describe the energy distribution of all electrons. The simplicity of the crystal structure, one atom in the primitive unit cell, indicates that the acoustic phonons are generated while the electrons are releasing their excess energy to the lattice. The equilibration in acoustic modes allows the use of another temperature for the lattice subsystem. However, in semiconductors with more than one atom in the primitive unit cell, optical phonons become the accepting modes and at least three temperatures have to be defined. Carriers more readily interact with optical phonons with a scattering time ($\tau_{\mathrm{e-ph}}$) typically of a few hundred femtoseconds [e.g., ~165 fs in GaAs (*20, 21*) and ~240 fs in Si (*22, 23*)], and the importance of this time scale on the observed nonequilibrium behavior will be addressed below. Finally, in a semiconductor, because of the existence of the band gap and the complex band structure, the highly excited carriers (electrons and holes) may not be able to reach Fermi–Dirac distributions on a femtosecond time scale and therefore, an electron temperature cannot be defined.

A.2. Carrier Excitation

Because lattice dynamics is initiated following the generation of carriers, it is important to examine the carrier processes in semiconductors; an overview of these processes and their optical probing has been provided (*24*). In short, charge carriers are created coherently on the femtosecond time scale with or without the assistance of lattice phonons, when photons of energy higher than the band gap impinge on a semiconductor surface. The coherence among electrons is lost in less than 10 fs at the carrier densities achieved due to the ultrafast carrier–carrier scattering. This results in featureless energy distribution of carriers around the excitation energy. The distribution may be additionally affected by other carrier excitation mechanisms, such as free-carrier absorption and impact ionization. However, the resulting spatial and energy distribution defines the initial condition for the following carrier and lattice dynamics.

The assumption of linear absorption is invalid in the regime of intense-field excitation. The band-filling effect (*25*), a manifestation of the Pauli exclusion principle, prevents an unlimited degree of vertical excitation through single-photon absorption (SPA); a comprehensive review for GaAs has been made (*26*). Carrier excitation through two-photon absorption (TPA), however, not only avoids such a saturation limit but also becomes crucial in influencing the lattice, because these TPA carriers carry higher (above-gap) excess energy. For the fluences used in this study at 800 nm (Fig. 9), we deduced $n_{\mathrm{TPA}}(z=0) = 7.1$, 3.2, and 1.2×10^{19} cm^{-3}, much higher values than the saturated SPA carrier density (2.5×10^{18} cm^{-3}). Here, $n_{\mathrm{TPA}}(z=0)$ is the carrier density near the surface ($z = 0$) calculated with the use of the TPA coefficient and dependence of n_{TPA} on fluence under a similar excitation condition in the literature (*27*).

Carrier excitation by high-energy photons may be further influenced by ambipolar diffusion (*28*) and bleaching of the near-edge valence bands due to density-of-states consideration (*26*). The fast carrier diffusion greatly reduces the density near the surface even before any substantial energy transfer to phonons takes place. We estimate, by using the 1D diffusion equation

$$\frac{\partial n}{\partial t} = D\frac{\partial^2 n}{\partial z^2}$$

$$n(z,t) = \frac{const}{\sqrt{Dt}}\cdot\exp\left(-\frac{z^2}{4Dt}\right) \tag{1}$$

where D is the ambipolar diffusion constant (*29*), an initial density $n(z=0)$ of 10^{21} cm^{-3} by 266-nm light will drop to $<10^{20}$ cm^{-3} after $t = 200$ fs, which becomes comparable to the value of $n_{\mathrm{TPA}}(z=0)$ at 800 nm. In contrast, carriers generated by 800-nm light are much less affected by this diffusion because of the lower initial density (see above) and the large penetration depth (710 nm). Therefore, the similar maximum intensity reduction for the two wavelengths (266 and 800 nm) and the reverse (from thermal) trend of the maximum lattice expansion indicated in Fig. 7 can be rationalized based on the comparable carrier densities near the surface.

Optical studies have shown that intense carrier excitation by photons can strongly affect the electronic state of a semiconductor on the ultrashort time scale (*30*). It is important to point out that the observed equilibration time constant (7 ps) between carriers and the lattice matches well with the rise time for structural changes reported here, even though lattice dynamics was not directly seen in the spectroscopic probing.

A.3. Influence of Band Structures and Lattice Phonons

The dispersion of band structure plays an important role in the final nature of electron distribution. For GaAs, the different excitation wavelengths provide an opportunity to reach different regions and distribution. At 800 nm, the TPA process, which is much more important than the SPA process from Γ_{8v} to Γ_{6c}, occurs not only around the Γ region but also along the Λ direction close to the L_{6c} valley (*31*); thus, accumulation of electrons in the L valley is expected (Fig. 1b). At 266 nm, however, the photon energy matches the critical point E_0' $(+\Delta_0')$ which features the interband transitions through $\Gamma_{8v} \rightarrow (\Gamma_{7c}, \Gamma_{8c})$ and $\Delta_{5v} \rightarrow \Delta_{5c}$ near Γ (*32, 33*), and consequently, a large number of electrons will go to the X valleys after they release some excess energy to the phonons.

The consequence of having the charge carriers in different parts of the band structure is very important. Although essentially no lattice mismatch exists between GaAs and $Al_{0.6}Ga_{0.4}As$, they have different electronic band structures, and the inset of Fig. 1b shows the comparison of the band energies at three high-symmetry points. Thus, according to the heterostructure used in the reflection experiments, electrons at L_{6c} (from TPA at 800 nm) are energetically trapped in the GaAs quantum well, whereas those at X_{6c}

(from SPA at 266 nm) may still be able to diffuse across the $Al_{0.6}Ga_{0.4}As$ layer. As discussed in Sec. B.1 of Ch. 2, more carriers in the electronic excited states may induce significant weakening of the lattice potential and consequently larger lattice expansion as observed in UEC. It is therefore understandable that the large amplitude of expansion at 800 nm (Fig. 7b), compared with that of 266-nm excitation, is a natural result of this carrier trapping.

It is noted that the issue of quantum confinement (continuum vs the discreteness of energy states) arises when one or more of the dimensions of the sample has a size that is close to the bulk exciton electron–hole Bohr radius a_B; for GaAs, it was calculated to be ~12.5 nm (*34*), which is smaller but close to our GaAs layer/film thickness. Therefore, electrons at Γ_{6c} and light holes at Γ_{8v} may experience the confinement effect in the quasi-2D quantum well, since fewer electronic states will be available because of the quantization of allowed energies. However, in structural dynamics, at 266 nm and two photons of 800 nm, it is those high-energy carriers that are most responsible for the observations made here, and these carriers have energy-state structures with no discreteness. Thus, no confinement is expected, and indeed the close resemblance between $I(t)$ and $w(t)$ of reflection experiments at 266 nm (Fig. 3) and those reported in a previous study for bulk GaAs (*4*) confirms this conclusion for our heterostructure and also in transmission experiments. Thus, it is still a good approximation to treat the 20-nm thin layer/film of GaAs as a bulk material as far as the electronic structure is concerned.

Given the initial nonequilibrium state of the material structure, the question of significance is, what is the driving force(s) for the change on the ultrashort time scale. As mentioned earlier, the initially prepared carriers readily interact with optical phonons to transfer their excess energy on the time scale of few hundred femtoseconds. In a polar semiconductor like GaAs, longitudinal optical (LO) phonons are generated through the polar (Fröhlich) interaction with carriers, and this coupling is strongest for the long-wavelength (i.e., small-wavevector) LO phonons since the scattering rate varies as $1/q^2$ ($\boldsymbol{q}$ is the crystal wavevector) (*35*). As a result, more and more LO phonons are accumulated around the Brillouin zone center Γ. Concurrently, the carriers lower their average energy and in the process may occupy other regions of the band structure (e.g., the Γ, L, or X valley). Carrier diffusion can also be occurring in parallel.

Because of the dispersion relation, the LO phonons nearly undergo no propagation, and, thus, can only decay by the generation of other phonons through lattice anharmonicity. The major relaxation channel involves the generation of pairs of longitudinal acoustic (LA) phonons of half of the LO-phonon energy but with opposite $\boldsymbol{q}$, a requirement of the conservation of energy and momentum. The lifetime of a LO phonon, $\tau_{\mathrm{LO}\rightarrow\mathrm{LA}}$, is typically a few picoseconds (*20, 36*), and the generated LA phonons have a large $|\boldsymbol{q}|$ (i.e., a small wavelength), resulting in dynamical inhomogeneity/strain of the lattice because their wavelength is on the length scale of a unit cell. On the ultrashort time scale the distribution in $\boldsymbol{q}$ leads to propagation of a strain packet with the speed of sound, transporting energy away or toward the surface region of the solid. At room temperature, because of the existent thermal phonons ($kT \sim 26$ meV) populated in the acoustic modes, phonon–phonon scattering may take place and randomize the phonon distribution.

B. Nonequilibrium Structural Dynamics

In what follows, GaAs is used as a prototype system to address the nature of nonequilibrium dynamics in semiconductors on the ultrashort time scale. Numerous spectroscopic studies of carrier and lattice dynamics have in the past primarily focused on

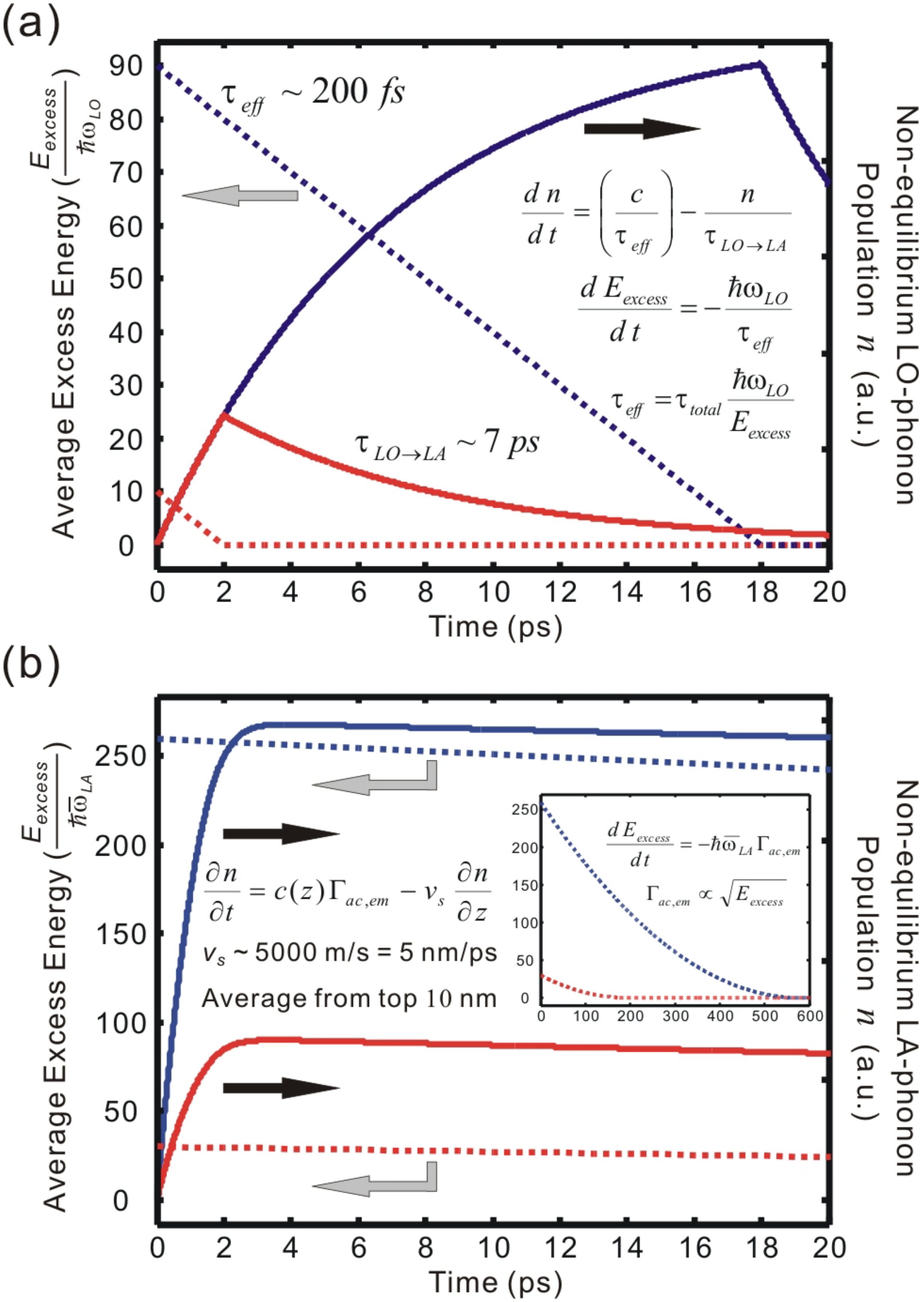

(See next page for the figure caption.)

Fig. 11. Theoretical calculations. (a) LO-phonon population at early times (solid curves). Nonequilibrium phonons are generated during the energy relaxation of carriers (which is governed by the second equation, if a stepwise relaxation mechanism is considered; dash curves). τ_{eff} is an effective LO-phonon generation time including the hot-phonon (phonon-reabsorption) effect. Depending on the initial excess energy (blue: 90 $\hbar\omega_{\mathrm{LO}}$ and red: 10 $\hbar\omega_{\mathrm{LO}}$) the overall time τ_{total} for LO-phonon population is given by the third equation. LO phonons can be converted into LA phonons in a time of ~7 ps, and therefore the LO-phonon population is governed by the sum of a positive generation term and a negative decay term, as shown by the first equation; c is a constant which is related to ratio of the carrier density over the number of optical normal modes active in the above-mentioned process. If most of the carriers transfer their excess energy to the lattice, no more source term exists for the generation of LO phonons, giving an exponential decay with the time constant of ~7 ps. (b) LA-phonon population at early times (solid curves) if the direct coupling between carriers and LA phonons is considered. The inset shows the average carrier energy as a function of time. Because the rate of this scattering is slow [on a picosecond time scale, and governed by two equations (*63*) in the inset], energy relaxation of carriers becomes a slow process. The acoustic phonons propagate at the speed of sound, as described by the second term of the equation on the left. Thus, acoustic phonons in the top 10-nm surface region will transit in 2 ps (10 nm divided by the sound velocity in GaAs).

optical and dielectric properties, such as Raman scattering for monitoring the generation and decay of small-q optical phonons (*20, 36*), and surface deflection spectroscopy for probing the generation and motion of LA phonons (*37*). Reflection transient grating (*38*), transient reflectivity, and dielectric function measurements (*30*) have also been introduced to study the lattice temperature and to describe the phonon/electron subsystems. The power of UEC is in its capability to monitor the transient motion and dynamical inhomogeneity of the structure itself.

B.1. Local Atomic Motions: Diffraction Intensity

In physical space, the vibrations of Ga and As atoms (optical phonons) are the first lattice motions generated following the optical carrier excitation, which can alter the structure and change diffraction intensity. As discussed in Sec. B.3 of Ch. 2, it is the vertical Ga–As vibrations along $\hat{n}$ that are responsible for the change, and the more optical phonons are generated, the larger the average amplitude of this vibration and change will be present in the crystal. Indeed, Figures 4 and 6b show that, regardless of the excitation wavelength, reduction of the (008) spot intensity always proceeds ahead and faster than changes of other diffraction features, the spot movement and width change.

The time scale for these local motions is picoseconds. For a range of 0.5 eV of excess energy, the scattering time $\tau_{\text{e–ph}}$ was found to be 165 fs at a low carrier density (*20*), and assuming the same $\tau_{\text{e–ph}}$ for our excess energy (3.23 eV) we can estimate the total time for the intensity loss. Because $\hbar\omega_{\text{LO}}$ = 36 meV, 90 such phonons will be emitted during the process, predicting the rise time to be 90 times 165 fs, which is ~15 ps. However, during such a process, the conversion to acoustic packets may occur and according to optical studies, this conversion takes ~7 ps for GaAs (*20, 30, 36*). Figure 11a

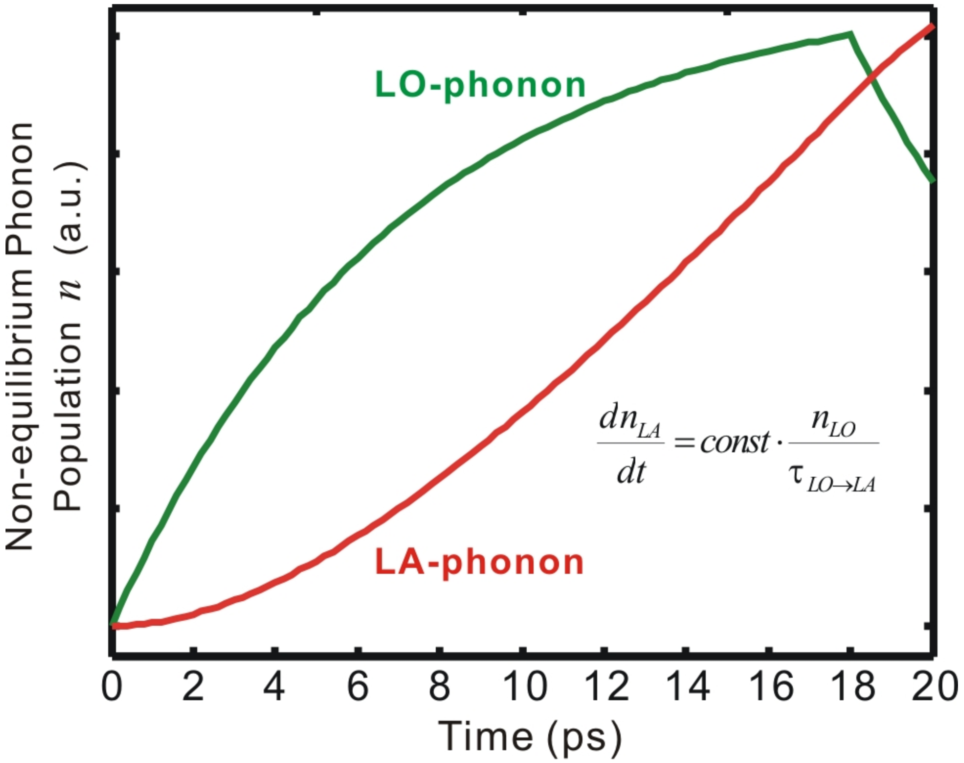

Fig. 12. Comparison of LO and LA-phonon populations at early times. Because of the relatively large LO-phonon lifetime (~7 ps), LA-phonon population rises but with a delay relative to the LO-phonon rise. The direct conversion relationship indicates a similar rise time for both populations.

shows the theoretical results for the generation and conversion of LO phonons which have similar time scales (15 and 7 ps); Figure 11b considers the dominance of acoustic process, and in this case, the rise is simply determined by the speed of sound. Other processes can contribute to the slowing down of the rise, and these include the hot-phonon (phonon-reabsorption) effect (*39*), intervalley scattering (*40, 41*), and screening of the carrier–phonon coupling (*42*). The UEC results provide the experimental evidence for the direct role of lattice motions by optical and acoustic phonons.

As shown in Fig. 4, the intensity drop occurs at an earlier time than the width (and also the Lorentzian component) change, but the slope is nearly the same. This behavior indicates that the observed time lag is a direct measure of the conversion of optical-to-acoustic lattice motions, as the width change must be delayed until dynamical inhomogeneity begins with acoustic/strain propagation; in Fig. 12, the change in population is shown for both LO and LA phonons, and the origin of the time delay is clear. The rise time is observed to be ~10 ps, and this is entirely consistent with the motion responsible for the change being that of optical phonons; it is noted that in Fig. 11b, the rise due to acoustic wave propagation (v_s ~ 5000 m/s along ⟨001⟩ directions) takes place in ~2 ps, shorter than the 10-ps rise.

With the use of the structure factor, $F(008)$, the maximum amplitude of the atomic vibrations along $\hat{n}$ can be estimated from the maximum intensity reduction at $t = 25$ ps (Fig. 7a). Using Eq. 35 of Ch. 2 and a drop of 30% in intensity, ±0.096 Å is obtained for the additional (nonthermal) vertical amplitude for each atom's motion around the equilibrium position (see Appendix A). It is equivalent to a 13.5% change of the vertical Ga–As distance ($a/4 = 1.413$ Å), a percentage close to the Lindemann stability limit (*43*). Experimentally, at a fluence just above the ones we used to conduct our experiments, we observed diffraction changes that did not recover fully, and this long-term deterioration of the material indicates that the damage threshold has been reached. Accordingly, the experimental observations of the intensity change, both the time scale and amplitude, are consistent with theoretical calculations.

For the case of intensity reduction in transmission, the estimation of maximum vibrational amplitude can also be made. It is noticed that the ~10% intensity decrease of the (080) spot in transmission (Fig. 10c) was less than the ~30% of the (008) spot in reflection (Fig. 3a) even though the excitation fluences were somewhat larger in the former case. This difference is due to the fact that the transmission experiments were performed with a small crystal rotation of 2°, and thus, the projection of the vibrational amplitude onto the scattering vector ***s*** is relatively small. The linear relation obtained in Fig. 10d between the intensity decrease and s^2 provides a slope that gives $\Delta\langle u^2\rangle_{\text{projected}} = 0.0015\pm0.0002$ Å^2, a measure of the (projected) increase in the mean-square amplitudes $\langle u^2\rangle$ of vertical atomic vibrations. We estimate $\Delta\langle u^2\rangle \sim \Delta\langle u^2\rangle_{\text{projected}}/\sin 2°$ to be 0.043 Å^2, a value which is even larger than $\langle u^2\rangle_{\text{total}}$ of the thermal motion in all directions at room temperature (*44*). Unlike the incoherent, random thermal motion, this additional vertical amplitude is due to the LO phonons generated within the first tens of picoseconds. The resulting increase in the vibrational amplitude for each atom along $\hat{n}$ is ~0.15 Å, which is comparable to the value obtained from the reflection experiments.

B.2. Potential-driven and Anisotropy of Lattice Expansion

The objective here is to understand the time scale, anisotropy, and the amplitude of lattice expansion. First, the optical excitation of GaAs(001) at 266 nm is considered. Initially, the carriers are generated in the excited states near Γ, which means that the electronic wavefunction (Bloch function) has a near-zero crystal wavevector; the positive phase character between neighboring unit cells is preserved, whether or not Ga and As atoms are in the bonding (ground) or antibonding (excited) state, and therefore, lattice expansion at this electronic configuration is not expected. As the carriers transfer their excess energy to optical phonons, they reach different electronic states whose Bloch functions have larger crystal wavevectors, particularly, in this case, along the ⟨001⟩ directions (Fig. 1b). The phase modulation in the wavefunction (with pluses and minuses) along a certain direction indicates that, when carriers occupy these electronic states, unit cells can be modified through the new crystal potential, which leads in this case to a

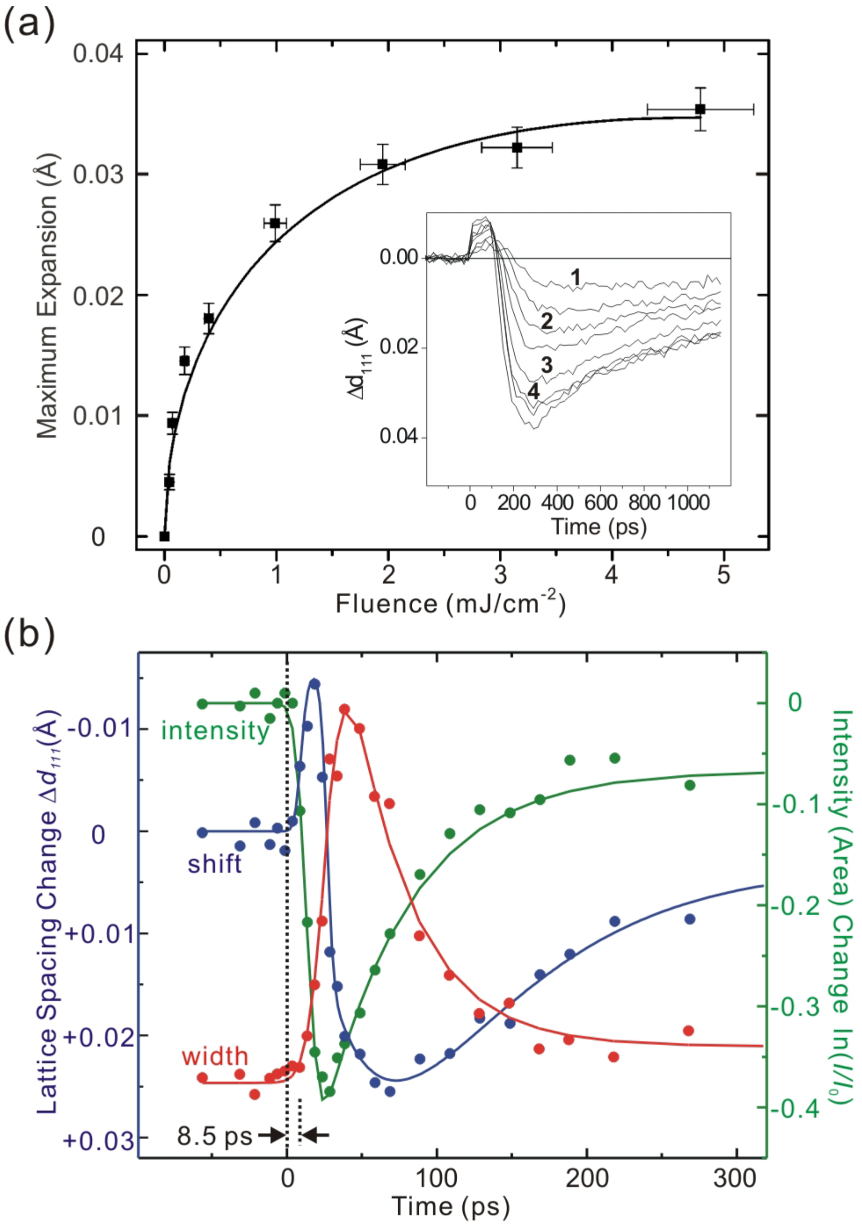

Fig. 13. UEC of single crystals (Ref. 4). (a) Maximum lattice expansion $\Delta d_{111}(t)$ as a function of fluence for 266-nm excitation; the inset shows the overall temporal behavior. Saturation of the maximum expansion at high fluences is evident. (b) Temporal behavior of the (222) spot intensity (green dots) and width (red dots) change, together with that of the "derived" lattice spacing change (blue dots) from the spot position shift. Again, a delay in the width change relative to the intensity drop can be clearly seen. The small amplitude peak in the spot movement at early times is discussed in Text.

weakening of the lattice in the [001] direction. As more and more carriers reach the energy states in the X valley, the larger the potential-driven lattice change will be along the $\hat{n}$ ($\hat{n} = [001] = \mathrm{X}$) direction. The relaxation of such carriers is mediated by optical-phonon emission, and hence, the rate of this process determines the time scale of both phonon generation and lattice expansion.

Indeed, as shown in Fig. 4, the similar rise time for both intensity reduction and lattice expansion confirms this potential-driven picture. Excitation fluence at 266 nm does not change this rise time (Fig. 8a), which is also expected because the time scale for the above-mentioned carrier relaxation does not strongly depend on the carrier density. As for the case of two-photon excitation by 800-nm light, more electrons are generated around the L_{6c} valley (the $\langle 111 \rangle$ directions) and therefore the weakening of the crystal potential along $\hat{n}$ is less effective. The lattice expansion being delayed and slower than the intensity reduction (Fig. 6b) can now be understood as due to the ineffective potential weakening, and/or because of an additional time for intervalley scattering from L to X (see below).

The nonlinear relationship between the excitation fluence at 266 nm and the maximum lattice expansion, as shown in Fig. 13 (adapted from Ref. 4), can also be explained by this potential-driven picture. Due to the rapid increase of the ambipolar diffusion constant as the carrier density becomes very high (*29*), the carriers at a higher fluence will undergo faster diffusion away from the surface region. Therefore, the "efficiency" of making a crystal expand at a high excitation level is greatly reduced; fluence higher than the damage threshold will cause irreversible structural changes. As to the case of 800-nm excitation in this study, because of the heterostructure which hinders diffusion of the carriers in the GaAs layer, the maximum expansion is still in proportion to the fluence used (Fig. 9a). Without the heterostructure, we shall expect a similar fluence dependence of the maximum expansion to be observed at 800 nm as that at 266 nm.

Summarizing, the expansion of the atomic motions along the $\hat{n}$ direction is due to a nonequilibrium state of the lattice influenced by the anisotropy of the potential. From Fig. 7b, a maximum lattice expansion of 0.022–0.042 Å is observed, which corresponds to a 0.4–0.8% change, much larger than the thermal limit; from intensity reduction, we know the structural changes are near the Lindemann limit, as discussed in Sec. B.1 in more detail. The rise of this change occurs in ~10 ps and with the changes in intensity, as discussed above. We note that structural changes by electronic excitation, with nuclear motions, have been studied by optical (*45, 46*), x-ray (*47-50*), and electron diffraction (*51, 52*) methods. However, in the present contribution, we provide the first reported reversible potential-driven structural changes mapped with its anisotropy and lattice-induced changes, using UEC. The effect of radiative recombination and nonradiative Auger processes is considered in Appendix B. The similar rise time (~10 ps) for the development of diffraction changes made at different fluences, wavelengths, and detection geometries confirms the minor role of these two carrier processes which are density-dependent.

In general, the probing of the anisotropy of lattice expansion discussed above is sensitive to the geometry of the experiment. Given the experimental excitation surface area relative to the penetration depth along $\hat{n}$, the horizontal 2D spatial distribution is more uniform (Gaussian-type, bulge on the micrometer or larger scale) compared to the vertical one (excitation penetration depth of nanometer scale). For such a case, the temperature/carrier density gradient in the $\hat{n}$ direction would be expected to lead to more expansion along $\hat{n}$ when compared with lateral expansion. However, as shown above for both the 266 nm (nanometer penetration) and 800 nm (micrometer penetration), the vertical expansions were similar, and in both cases, no lateral expansion was observed. Thus, the important cause of the anisotropy, besides the potential change, is the fact that the surface has no restriction (stress-free) in the vertical direction and is free to expand. The contributions to vertical expansion from different “bulk” stresses integrate at the surface. On the time scale of UEC, we did not observe a horizontal lattice expansion either in the reflection or in the transmission geometry, and these observations are evidence of anisotropic, nonthermal expansion.

B.3. Dynamical inhomogeneity: Width and Shape

When the inhomogeneity is caused by acoustic waves of relatively short wavelength (at $\pm\boldsymbol{q}$), their downward propagation at the speed of sound would decrease their population in the probed surface region; in 2 ps, they can move across a 10-nm length which is on the order of the probed depth. Within the excited (different densities) range, the upward propagation brings the waves generated “inside” the crystal toward the surface, and the net effect is the vertical atomic motions with the surface atoms experiencing the largest change. Ultimately, phonon–phonon scattering will lead to a broadened, randomized distribution in the acoustic modes. Thus, besides the expansion of the lattice, which results in a decrease in the position of diffraction spots (lower s), diffraction broadening due to this dynamical inhomogeneity of lattice spacings is expected.

As shown in Sec. B.2 of Ch. 2, the temporal changes in the spot width and shape are both related to the lattice inhomogeneity, and it is not surprisingly that $w(t)$ and $\eta(t)$ have a similar behavior over the entire temporal range (Fig. 4, inset). Because of the direct relationship in the generation of LO and LA phonons, $w(t)$ is also expected to closely follow $I(t)$, which is confirmed by our observations. At this point, we would like to emphasize that the temporal behavior of $w(t)$ is a consequence of coherent intrinsic structural dynamics, and not simply an artifact due to inhomogeneous sum of contributions from areas of different excitations. We should have observed a very similar temporal behavior for $w(t)$ and $\Delta d_{001}(t)$ if the inhomogeneity were to be static in nature.

It is important to note that the observed dynamical inhomogeneity mostly appears along $\hat{n}$, and not in the 2D plane. As shown in Fig. 5a, the horizontal width change is much smaller and behaves like a step function with time, indicating a relatively very small lattice inhomogeneity along the 2D directions. The anisotropy is evident, and its magnitude is in parallel with a genuine dynamical inhomogeneity, i.e., the larger the change in lattice spacing, the larger the inhomogeneity. This phenomenon is due to the fact that the surface is free of stress compared to the constrained 2D horizontal lattice. Consistent with this picture, Figure 8b shows that the maximum width change is linearly proportional to the fluence at 266 nm, but the temporal behavior remains the same. In the case of 800-nm excitation, due to the nonlinear TPA in GaAs and the heterostructure underneath, a similar linear relationship is not expected. In the following discussion, these differences in temporal behaviors will become clear.

C. Restructuring at Long Times

From all experimental results obtained in the reflection detection mode, it is apparent that there is a temporal recovery of the nonequilibrium structures. This recovery is due to the transfer of excess energy away from the probed region into the bulk, either through carrier diffusion or through lattice relaxation by acoustic energy propagation and/or thermal diffusion. Further examination of the fast recovery of $I(t)$, $\Delta d_{001}(t)$, $w(t)$, and $\eta(t)$ (inset of Fig. 4 and Fig. 6b) shows that they share a similar profile after reaching the maximum. At higher fluence or shorter excitation wavelength, the recovery is even faster in the relatively short-time regime with an apparent time constant as short as 30–40 ps (Fig. 4, inset). The recovery is not observed in transmission experiments because the sample is very thin and there is no dissipation of energy on our time scale.

In order to pinpoint whether the carrier or phonon subsystem is responsible for the observed initial fast decay, it is helpful to first consider the case where there are no carrier and thermal diffusion, a hypothetical situation. For this case, one would expect the crystal structure to recover to its equilibrium state only by the optical-to-acoustic phonon conversion (in ~7 ps) with the acoustic waves propagating into the bulk. As a result, all four diffraction features $I(t)$, $\Delta d_{001}(t)$, $w(t)$, and $\eta(t)$ would return to their corresponding equilibrium values in only ~7 ps, contrary to the experimental results which show fast and slow decays on the picosecond and nanosecond time scales.

Because carriers continue to produce more optical phonons and concurrently undergo ambipolar diffusion, which gradually reduces their density in the surface region, the remaining carriers continue to be the heat source for the lattice. This process influences the dynamics of recovery in the initial phase, and it is reasonable that $I(t)$, $\Delta d_{001}(t)$, $w(t)$ and $\eta(t)$ all recover with the same profile on this time scale. Studies of wavelength and fluence dependence of the profile support this picture. Rapid structural recovery can be seen most prominent in the high-fluence 266-nm data (Fig. 4, inset) because carrier diffusion is significant at this high carrier density which is confined in a narrow spatial distribution of $\delta \sim 6.4$ nm (inverse of the absorption coefficient). Decreasing the fluence at 266 nm does not significantly alter the initial recovery time because carrier diffusion is still dominant for the nanometer-scale excitation; the smaller

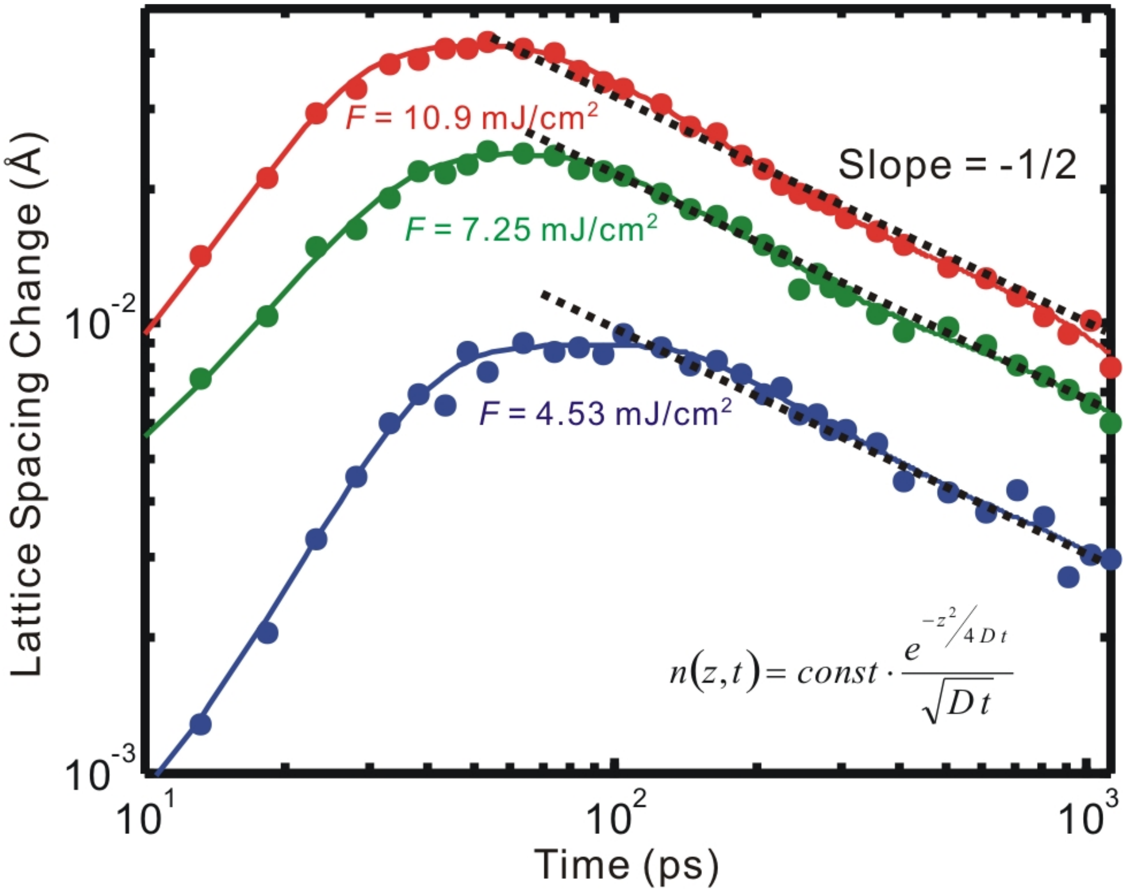

Fig. 14. Lattice spacing change as a function of time and fluence at 800 nm. In Text, the direct connection between the extent of lattice expansion and carrier density at the surface is discussed. The linear decay of lattice expansion with the slope of –1/2 in the log–log plot, together with the fluence dependence, provide strong support of restructuring under the influence of carrier diffusion on the shorter time scale and/or thermal diffusion on the longer time scale.

the excitation thickness, the faster the diffusion (for density effect, see Sec. B.2).

For 800-nm experiments, if the fluence is high, fast recovery of the system is noticeable because of the large TPA carrier density (Fig. 9, red and green curves). It is noted that the spatial distribution of TPA carriers depends on the excitation intensity: the effective absorption coefficient of TPA is $\beta I \sim 1.8 \times 10^4$ cm^{-1} at the highest fluence used at

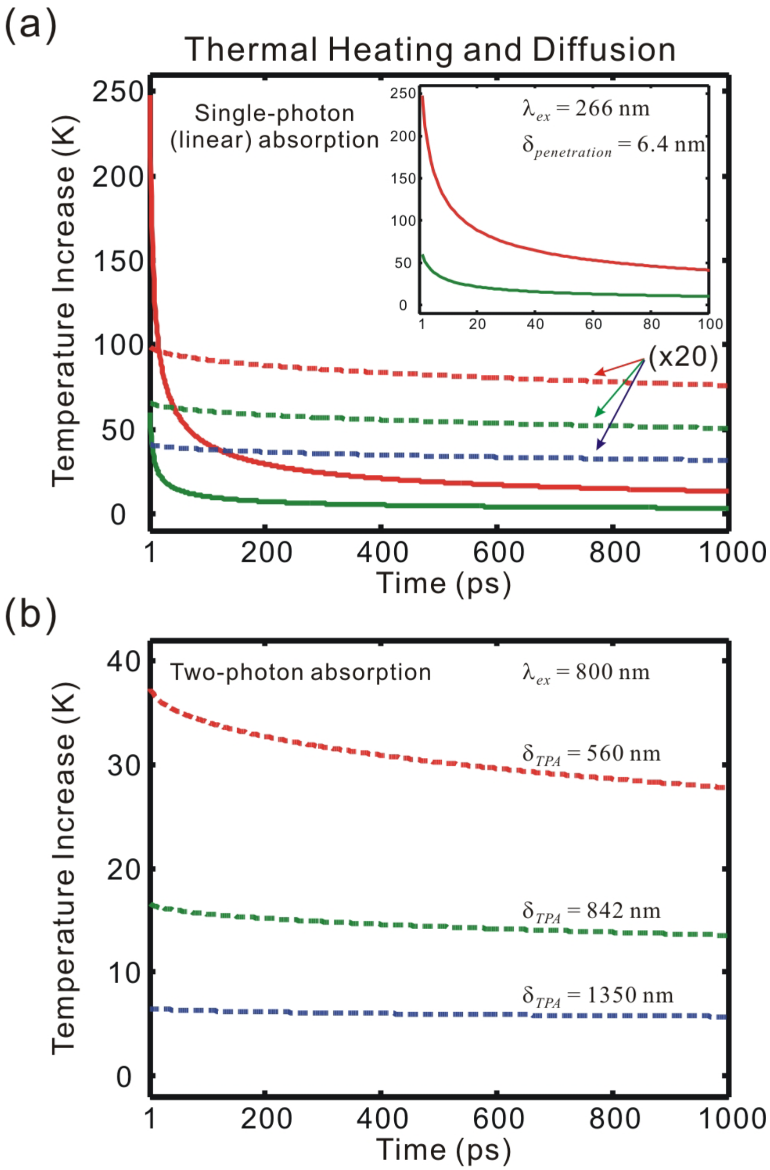

Fig. 15. Heat diffusion. Theoretical lattice temperatures at the surface as a function of time when heat diffusion is considered at the two wavelengths (266 nm, solid lines; 800 nm, dash lines) and the different fluences used. (a) The cases of linear (single-photon) absorption with no band-filling effect; the initial temperature increase is determined by Eq. 34 of Ch. 2. The fast decay is obtained for the 266-nm excitation because of the small penetration depth (the inset shows the early-time behavior). At 800 nm, the surface temperature increase is very small and its decay is very slow, showing a totally different temporal behavior from the 266-nm case, contrary to experimental observations. (b) The cases of TPA at 800 nm; the initial temperature increase is still limited because the excitation region is sub-micrometer to micrometer size. The temperature relaxation is also very slow and totally different from the 266-nm behavior.

800 nm [since $\beta = 210$ cm/GW for our experimental geometry (*27*)] and the penetration depth is estimated to be ~560 nm (SPA carriers are barely affected by diffusion because of saturation within a thickness of tens of micrometers). As the fluence becomes small, however, the number of TPA carriers is greatly reduced, and the excitation spatial distribution becomes essentially flat inside the crystal. Since carrier diffusion is not as important in such cases, fast recovery becomes less distinct or even disappears (Fig. 9, blue curves). Similar results of wavelength and fluence dependence were obtained for silicon using UEC (compare Fig. 4e in Ref. 3 with the red curve in Fig. 5b in Ref. 6), and the above-mentioned physical picture is similarly applicable.

Figure 14 presents an important observation which supports this picture. The slope of the linear decays over time, up to 1 ns, in the log–log plot is –1/2, consistent with the behavior predicted by Eq. 1; near the surface, $\log n(0,t) = (-1/2)\log(t) + \text{constant}$. Because of the heterostructure, diffusion of the TPA carriers at 800 nm can be hindered, but eventually, the system returns to the ground state. On the sub-nanosecond to nanosecond time scale, the relaxation may take place through carrier–carrier scatterings and the (slow) Auger process: some carriers will acquire more energy than others and overcome the energy barrier to diffuse. For 266 nm, in addition to diffusion, the decay has a manifestation of interband conversion, as discussed above.

At longer times, restructuring of the lattice proceeds through thermalization among the vibrational modes. As mentioned earlier, phonon–phonon scatterings of acoustic modes can result in randomization of the phonon distribution and therefore thermalization of the lattice. The relaxation of lattice vibrations may then share some resemblance to the process of heat diffusion. Figure 15 shows results of the theoretical solutions (*53*), using parameters given by our experimental conditions, to the heat diffusion equation:

$$-k\,\frac{\partial^2 T(z,t)}{\partial z^2} = -\,C_l\,\frac{\partial T(z,t)}{\partial t} + \frac{F_{\mathrm{heating}}}{\sqrt{\pi}\,\delta\,t_{\mathrm{p}}}\,e^{-z/\delta}\,e^{-\left(t/t_{\mathrm{p}}\right)^2} \tag{2}$$

where k is the thermal conductivity (a constant for a cubic lattice) and t_{p} is the laser pulse duration, which is 120 fs divided by $2(\ln 2)^{1/2}$; see Eq. 34 of Ch. 2 for other notations. Equation 2 shows that the higher the heating fluence (F_{heating}), the larger the initial temperature rise; it also shows that the temperature profile into the bulk $T(z)$ and its temporal evolution $T(t)$ are dependent on the penetration depth δ. The purpose of Fig. 15 is to show that, besides the failure of the thermal-heating picture to describe the nonequilibrium dynamics in semiconductors, heat diffusion is a very slow process and only becomes more important on the nanosecond or longer time scale. It is noted that comparison of the results in panels a and b of Fig. 15 for 266 and 800 nm excludes thermal diffusion as a mechanism for restructuring at short times (for the 266-nm excitation). This is because the same process would predict the absence of the fast component at 800 nm, contrary to experimental observations. However, at longer times (e.g., after 200 ps), thermal diffusion cannot be ignored.

When the residual amplitude of the diffraction changes at $t = 1$ ns are examined, one notices that more decay in $w(t)$ and $\eta(t)$ has occurred when compared with that in $I(t)$ and $\Delta d_{001}(t)$. For example, the high-fluence 266-nm data shows that $w(t)$ and $\eta(t)$ have fully returned to their negative-time equilibrium values even before $t = 1$ ns, whereas at $t = 1$ ns, $I(t)$ and $\Delta d_{001}(t)$ are still decaying with 18% and 6% of the corresponding maximum changes (Fig. 3). This $w(t)$ and $\eta(t)$ behavior indicates that dynamical inhomogeneity has vanished on this time scale. The larger residual $I(t)$ (determined by atomic vibrational motions) relative to that of $\Delta d_{001}(t)$ (affected by excited carriers) is consistent with heat conduction being in general a slower process than carrier diffusion. From the 800-nm data, we find that the residual changes in $I(t)$ and $\Delta d_{001}(t)$ at $t = 1$ ns, for each fluence, have very comparable percentage with respect to their maximum values. It is because more photoinjected carriers are confined within the GaAs layer, and hence, the relaxation becomes more difficult such that $\Delta d_{001}(t)$ recovers relatively slowly, even on a sub-nanosecond time scale.

Concluding Remarks: UEC and Structural Dynamics

In the present work, we have demonstrated the capability of UEC to study structural dynamics with combined atomic-scale spatial and ultrafast temporal resolutions. By monitoring changes of the diffraction features (Bragg spots, intensity, width and its homogeneous contribution) at different times, following an "ultrafast heating" of the material, we are able to map out the nature of atomic motions and the time scales of the processes involved: electronic and nuclear at ultrashort times and diffusion at longer times. Structural changes in the nonequilibrium regime and restructuring toward equilibrium are features that were examined in detail. The kinematic description for diffraction, as provided in Ch. 2, is shown to be sufficient for unraveling structural changes in these condensed-matter studies (thin crystals and relatively low atomic numbers). For this and other reasons, important aspects of the theory needed were highlighted in order to obtain structural and dynamical information from diffraction patterns recorded in the reflection and transmission modes of UEC.

One important general finding of this study, which is relevant to others (*3, 4*), is the universality of the structural–temporal behavior. Typically, following the ultrafast heating through carrier excitation of the material, a large change (for cubic GaAs,

$\Delta d_{001}(t)/a = 0.75\%$ at 800 nm) in lattice expansion is observed on the ultrashort time scale, far beyond any thermal expansion: because $\alpha_l = 5.73\times10^{-6}\ \mathrm{K}^{-1}$, this expansion would translate into a temperature rise of ~1300 K. Similar large changes are observed for the intensity drop and width increase. Moreover, the change occurs with a time constant of ~10 ps, and, remarkably, is highly anisotropic; it occurs in the direction normal to the surface. The anisotropy is the result of accumulated surface stress and lattice-potential change as discussed in Sec. B.2 and below.

For the case studied here, the change is prompt for the intensity drop and the Bragg spot movement, but is delayed by ~7 ps for the width and its homogeneous (Lorentzian) contribution. Following the maximum change, these diffraction features reverse the change and take on values in the direction of pre-heating equilibration. We examined in depth this behavior for GaAs as a prototype system and provided a summary of results of numerous experiments made under different conditions: fluence and wavelength of the heating pulse, angle of incidence for the probing electrons (rocking curves), sample thickness and composition, and detection mode (reflection or transmission). In this regard, the study made here on the quantum-well heterostructure (20-nm GaAs on top of 50-nm $Al_{0.6}Ga_{0.4}As$ over 450-μm GaAs) proved essential because of its nanometer-scale structure and the difference in the band structure (Fig. 1b, inset).

The emerging physical picture of structural dynamics defines the following concepts. A general one refers to the nature of the structure following ultrafast heating: a large nonthermal change in a nonequilibrium state. This state cannot be reached by incoherent thermal heating of atoms. It is reached because the excited carriers of the material lower their energy (through the electron–phonon coupling, $\tau_{\mathrm{e-ph}} \sim 165$ fs) by generating well-defined vibrations of atoms in the unit cell (optical phonons) and such deformations produce, by anharmonic couplings, acoustic waves in a few picoseconds (~7 ps for GaAs). Such deformations lead to large-amplitude motions of the lattice, with a distribution of distances (dynamical inhomogeneity, as opposed to distribution of static structural deformations; see Sec. B.2 of Ch. 2). The wavevector of the acoustic packet is relatively large, for energy and momentum conservation, and its short wavelength makes the change on the scale of lattice spacings. This picture for a semiconductor contrasts that of a metal, with one atom in the primitive unit cell, and for which the carriers directly generate these stresses (forces) of acoustic wave propagation.

The consequences of this nonequilibrium behavior are a large change in lattice spacing (Bragg spot movement) and a large decrease in intensity, both without delay since the vertical optical-phonon deformations occur within 165 fs for each phonon. At our excess energy, 90 such phonons results in a total time of ~15 ps for the maximum change. In contrast, the increase in width (dynamic inhomogeneity), although also large, is delayed by ~7 ps, the time scale for conversion to acoustic waves. This behavior is clearly evident in our UEC results (see Figs. 4 and 6b). It is noted that acoustic wave propagation through a 10-nm material takes only ~2 ps since the speed of sound in GaAs is 4731 m/s along the [001] direction.

Another important concept is what we term potential-driven change and anisotropy. Through this unique heating with “three temperatures” of the electrons, lattice-optical, and lattice-acoustic modes, it is important to emphasize the role of carriers in changing the potential and the associated anisotropy. The initial carriers are prepared with a crystal momentum (wavevector) near the zero value (all phases are positive). However, depending on the band structure, carriers can reach other regions with a different crystal momentum, with a phase combination that characterizes a given lattice direction. Now the atoms experience a different potential of weaker bonding and this antibonding character (± phases) facilitates the subsequent nuclear motion in that direction. Thus, such schemes of excitation open the door to studies of “controlled heating” of nonequilibrium structures. This is to be contrasted with heating of metals with a T jump in a lattice through a two-temperature (electron and lattice) scheme; in such cases, the electrons have a much higher temperature than the lattice because of their poor heat capacity, but they equilibrate with the lattice in 1–2 ps. It is important to realize that heating through carriers, although it might have a much smaller occurrence in thermal experiments, cannot be ignored at steady state (infinite time scale); it is certainly of great significance to femtochemistry of catalysis (*18*), and to electronic structural changes with little or no lattice phonon motion (*45, 46*). In general, the anisotropy will result from the free-surface (in contrast to lateral bulk) expansion due to the temperature/carrier density gradient and the potential-driven (antibonding character) change, and both will be prominent at short times.

Toward equilibration, the structure at ultrashort time cools down primarily by diffusion of carriers at early time and also by thermal diffusion on the nanosecond (and longer) time scale. Energy redistribution among modes will not alter the average energy, but if some modes are selectively probed (or excited), then the redistribution will contribute to the decay. The evidence for carrier diffusion, especially at early times, comes from the fact that thermal diffusion at the two wavelengths studied would have entirely different behavior (Fig. 15) at short time (because of difference in penetration length), contrary to the experimental observation. The observed $1/\sqrt{t}$ behavior (Fig. 14) for the restructuring is also consistent with the diffusion of carriers and its fluence dependence. Heat diffusion occurs at longer time (*54*). In the transmission mode, thermal diffusion is extremely slow in the thin samples used, and indeed, we did not observe restructuring on the sub-nanosecond time scale. We also considered depletion of population by other processes, such as Auger and radiative recombination which scale with density (n^3 and n^2, respectively), but they are negligible particularly on the time scale below hundred(s) of picoseconds.

The observed nonequilibrium dynamics of the quantum-well heterostructure is similar to that of chlorine-terminated GaAs(111) (*4*), except for an early-time behavior in the Bragg spot position. Prior to expansion of the lattice there is a relatively small peak that shows the opposite behavior (Fig. 13b). This upward movement in s space may imply a decrease in lattice spacing, opposite to expectations of heating and carriers' weakening of bonding. However, the presence of a chlorine monolayer changes the surface characteristic. After carriers are excited, chlorine atoms will attract the electrons (electronegativity) and therefore a more repulsive surface potential may result in the formation of a diffraction spot at a slightly higher s value. The duration of this initial behavior may provide the time scale of charge separation, and as it diminishes, the normal downward movement of diffraction spot due to lattice expansion is observed. We cannot exclude the role of chlorine electronegativity in inducing polarization and initial contraction of the lattice.

In this comparison with single-crystal dynamics, the following points are noted. First, the width change obtained for single crystals is similar to that for the quantum-well structure; it is delayed from the intensity change. The apparent delay of the spot position (Fig. 13b) is misleading in view of the two, positive and negative, contributions present. Second, in all these studies, the intensity change and spot movement change are similar in profile, and this excludes the notion that spot movement may be due to an artifact caused by change in electron beam trajectory. This is further confirmed by recording changes of the direct electron beam position which was found to be relatively very small and, if any, occurred in opposite direction (see the Results and Analysis Section), indicating the negligible change of crystal (surface) potential in the presence of the heating pulse. Third, unlike the heterostructure with a well-defined nanometer layer and the absence of the chlorine monolayer, bulk material may exhibit the effect of diffraction/refraction in that, given the grazing reflection geometry, an electron beam incident at a spatial position distant from the heated area may be reflected by the underneath crystal planes and pass through (refracted by) the heated region (of different density from the underneath unexcited/less excited region) while exiting the crystal. This indirect interaction could lead to movement of the spot in the opposite direction but still gives rise to the same temporal profile as that of heating one. Care has to be taken to optimize the spatial and temporal overlaps, which had been fully developed for UEC experiments in our laboratories (see Ch. 3). Finally, it is noted that the thickness of the heated “bulge” is on the order of one angstrom, and the movement of spots is indicative of this expansion. Although such a bulge may have a significant consequence on the beam deflection direction in optical reflection experiments, the angstrom displacement causes a negligible effect to the shadow edge in our geometry.

With the same picture, it is straightforward to understand the phenomenon of ultrafast melting. As discussed earlier (Sec. B.1), at high fluences, both the atomic vibrations, with amplitudes near the Lindemann stability limit, and weakening of the crystal potential are induced. The high density of carriers may seriously affect the stability of the crystal structure, and the induced lattice motion may become too large for the surface to maintain its crystallinity. As a result, melting can be observed in the development of Debye–Scherrer rings, instead of Bragg spots; if surface evaporation occurs, the pattern will disappear. Such an ultrafast melting process is again potential-driven and far from being thermal. For polycrystalline silicon, studies of 2D melting were made with UEC (*3*).

Another study of polycrystalline silicon has also been reported with the use of time-resolved electron diffraction in transmission geometry (*55*). In contrast to the study reported here for single crystals (and quantum wells), whose structural dynamics are from a homogeneous lattice, the polycrystalline silicon dynamics must take into account the inhomogeneity of structures and the influence of this sample morphology on the carrier–lattice interaction. Moreover, the photogenerated carrier density in the reported study (*55*) was about one to two orders of magnitude higher than ours (due to the more efficient excitation and the lack of carrier diffusion), resulting in carrier screening and lengthening of the time scale for the electron–phonon coupling. The overall time scale is a few picoseconds, which is still comparable to our observation made in the transmission mode.

In conclusion, the methodology of UEC opens up new opportunities in the studies of materials and interfaces, as can be seen from the following chapters. The far-from-equilibrium structures observed in UEC cannot be appropriately described either by thermal heat diffusion equations (*53*) or by the thermoelastic models (*56*) because they do not take into account the effect of electronic band structure, and in these models, the lattice temperature is only determined by the absorbed fluence and the electron–lattice equilibrium. According to the present study, by changing to a different semiconductor, or even systematically varying the chemical composition, the electronic band structure may be fine-tuned and used to control the state of nonequilibrium dynamics, e.g., faster response of structural changes along a particular crystal direction. Moreover, the use of heterostructures, or the limiting of substrate dimensions, can restrict carrier diffusion, allowing for the use of the substrate as a constant energy source in the studies of interfaces. In future applications, we will greatly benefit from the many investigations of electron crystallography of static structures in materials and biological systems (*57-60*), and from studies of surfaces made on longer time scales (*54*).

Appendix A. Amplitude of Vibrational Motion

The amplitude of the vertical Ga–As vibration (optical phonon) responsible for the intensity reduction of the (008) Bragg spot can be estimated using the structure factor

$$F(008) = f_{\mathrm{Ga}}\exp(-16\pi i z_{\mathrm{Ga}}) + f_{\mathrm{As}}\exp(-16\pi i z_{\mathrm{As}}).$$

Here, two approximations are made to simplify the calculation. First, the mass difference between Ga and As (atomic weight: 69.7 vs 74.9) is neglected, and therefore the two atoms oscillate around the equilibrium positions symmetrically, i.e., $z_{\mathrm{Ga}} = +\delta_z$ and $z_{\mathrm{As}} = 1/4 - \delta_z$ where δ_z is the vertical displacement (relative to the unit-cell length) of the atoms and the 1/4 is the relative position in the unit cell, i.e., (0, 0, 0) for Ga and (1/4, 1/4, 1/4) for As. Second, because of their similar atomic numbers, the atomic scattering factors f_{Ga} and f_{As} will be considered equal. Thus, the (008) spot intensity becomes $|F(008)|^2 = 4|f_{\mathrm{Ga/As}}|^2\cos^2(16\pi\delta_z)$ for different δ_z values; the thermal Debye–Waller damping is not included. The time dependence is in δ_z.

For a harmonic motion, i.e., when $\ddot{\delta}_z = -\omega^2\delta_z$, we have $\delta_z = \delta_z^{\max}\sin(\omega t)$ and it follows that $\mathrm{d}\delta_z = -\omega\,[(\delta_z^{\max})^2 - \delta_z^2]^{1/2}\,\mathrm{d}t$, where $\delta_z^{\max}$ is the maximum value of vibrational amplitude. We now can calculate the average (over half a period, since ω^{-1} is shorter than temporal resolution considered) of $|F(008)|^2$ which is given by

$$<|S(008)|^2> \propto < \cos^2(16\pi\delta_z) > = \int_{-\delta_z^{\max}}^{\delta_z^{\max}} \cos^2(16\pi\delta_z)\tfrac{dt}{d\delta_z}\,d\delta_z \Big/ \int_{-\delta_z^{\max}}^{\delta_z^{\max}} \tfrac{dt}{d\delta_z}\,d\delta_z$$

which is equal to $[1 + J(0, 32\pi\delta_z^{\max})]/2$, where J is the Bessel function of the first kind. The experimental diffraction intensity drop, $I(t)/I_0$, is given by the average $\langle\cos^2(16\pi\delta_z)\rangle$. Given that $I(t{=}25\text{ps})/I_0 \sim 70\%$ the amplitude $\delta_z^{\max} = 0.0169$ is obtained, which, when multiplied by the lattice constant ($a = 5.653$ Å), gives the real-space maximum displacement of 0.0955 Å. It is the additional (from thermal; $[\langle u^2\rangle_{\text{thermal}}/3]^{1/2} = 0.0728$ Å) vertical displacement acquired by ultrafast heating. It is interesting that this value is very close to $\Delta d_{001}^{\max}$ measured at 800 nm.

Appendix B. Radiative and Auger Recombination

Radiative recombination of carriers reduces not only the number of carriers but also the total energy in the carrier subsystem because the emitted photons carry energy away. The process is described by the equation $\dot{n} = \dot{p} = -B\,n\,p$, where n (p) is the density of electrons (holes) in the conduction (valence) band, and B is the bimolecular radiative recombination coefficient whose value is typically on the order of 10^{-10} cm^3/s at room temperature (*61, 62*). It follows that the radiative decay rate $1/\tau_{\text{rad}}$ is given by Bn which, for an initial density of 10^{19} cm^{-3} (*53*), is ~10^9 s^{-1}. In 1 ps, the population decay will be negligible ($10^{19} - 10^{16} \sim 10^{19}$ cm^{-3}) Note that using carrier densities of order higher than 10^{19} cm^{-3} to calculate the rate will lead to false estimation because radiative recombination mostly occurs around the Γ valleys due to momentum conservation. In the case of 266-nm excitation, even though larger carrier densities may be created initially, their distribution over a much larger phase space and the band-filling effect exclude the possibility of having a faster radiative recombination rate; relaxation of electrons to Γ_{6c} becomes the rate-determination step but is blocked due to the Pauli exclusion principle by a filled quasi-steady-state valley. For an indirect-gap semiconductor material like Si, the rate will be even slower because the recombination requires the assistance of phonons. Hence, in general, radiative recombination has a negligible effect on the dynamics within the first nanosecond, a temporal range on which UEC focuses.

The nonradiative Auger recombination decreases the carrier density but retains the total energy, and the average energy of the remaining carriers increases. This process can be described by the equation $\dot{n} = -C_{\mathrm{p}}np^2 - C_{\mathrm{n}}n^2p$, where the coefficients C_{p} and C_{n} denote the Auger processes in the valence band and conduction band, respectively. Due to momentum conservation, those recombination events that involve crystal-momentum ranges other than the Γ valley will be less probable (*62*). Thus, through similar simple estimation, the Auger recombination rate is deduced to be $1/\tau_{\mathrm{Auger}} \sim C_{\mathrm{eff}}\, n^2 \sim 10^9\ \mathrm{s}^{-1}$ for an initial density near Γ of $\sim 10^{19}\ \mathrm{cm}^{-3}$ and C_{eff} of $7\times10^{-30}\ \mathrm{cm}^6/\mathrm{s}$ (*62*). This rate may be increased appreciably if the semiconductor materials are subject to very high fluences (*24*). However, for a UEC study in which the recovery of the system is necessary, such regimes are not desirable, so the Auger processes are expected to be on the sub-nanosecond time scale or slower. As discussed in Text, such a carrier relaxation mechanism does not interfere with the structural dynamics at early times.

References:

1. A. H. Zewail, *Annu. Rev. Phys. Chem.* **57**, 65 (2006).
2. R. Srinivasan, V. A. Lobastov, C.-Y. Ruan, A. H. Zewail, *Helv. Chim. Acta* **86**, 1763 (2003).
3. C.-Y. Ruan, F. Vigliotti, V. A. Lobastov, S. Y. Chen, A. H. Zewail, *Proc. Natl. Acad. Sci. USA* **101**, 1123 (2004).

4. F. Vigliotti, S. Y. Chen, C.-Y. Ruan, V. A. Lobastov, A. H. Zewail, *Angew. Chem. Int. Ed.* **43**, 2705 (2004).
5. C.-Y. Ruan, V. A. Lobastov, F. Vigliotti, S. Y. Chen, A. H. Zewail, *Science* **304**, 80 (2004).
6. S. Chen, M. T. Seidel, A. H. Zewail, *Proc. Natl. Acad. Sci. USA* **102**, 8854 (2005).
7. M. T. Seidel, S. Chen, A. H. Zewail, *J. Phys. Chem. C* **111**, 4920 (2007).
8. S. Chen, Ph.D. thesis, California Institute of Technology (2007).
9. D. von der Linde, *Annu. Rev. Mater. Sci.* **18**, 75 (1988).
10. J. Shah, *Ultrafast spectroscopy of semiconductors and semiconductor nanostructures* (Springer, Berlin, 2nd enlarged ed., 1999).
11. A. Konkar, S. Y. Lu, A. Madhukar, *Nano Lett.* **5**, 969 (2005).
12. N. Cavassilas, F. Aniel, K. Boujdaria, G. Fishman, *Phys. Rev. B* **64**, 115207 (2001).
13. M. E. Levinshtein, S. L. Rumyantsev, in *Handbook series on semiconductor parameters,* M. E. Levinshtein, S. L. Rumyantsev, M. Shur, Eds. (World Scientific, Singapore, 1996).
14. M.-G. Kang, S.-H. Sa, H.-H. Park, K.-S. Suh, K.-H. Oh, *Thin Solid Films* **308-309**, 634 (1997).
15. M. I. Kaganov, I. M. Lifshitz, L. V. Tanatarov, *Sov. Phys.-JETP* **4**, 173 (1957).
16. S. I. Anisimov, B. L. Kapeliovich, T. L. Perel'man, *Sov. Phys.-JETP* **39**, 375 (1974).
17. J. Hohlfeld *et al.*, *Chem. Phys.* **251**, 237 (2000).
18. G. Ertl, *Adv. Catal.* **45**, 1 (2000).
19. A. Othonos, *J. Appl. Phys.* **83**, 1789 (1998).
20. J. A. Kash, J. C. Tsang, J. M. Hvam, *Phys. Rev. Lett.* **54**, 2151 (1985).
21. H.-J. Polland, W. W. Rühle, K. Ploog, C. W. Tu, *Phys. Rev. B* **36**, 7722 (1987).

22. T. Sjodin, H. Petek, H.-L. Dai, *Phys. Rev. Lett.* **81**, 5664 (1998).

23. A. J. Sabbah, D. M. Riffe, *Phys. Rev. B* **66**, 165217 (2002).

24. S. K. Sundaram, E. Mazur, *Nat. Mater.* **1**, 217 (2002).

25. Y. H. Lee *et al.*, *Phys. Rev. Lett.* **57**, 2446 (1986).

26. J. S. Blakemore, *J. Appl. Phys.* **53**, R123 (1982).

27. F. Kadlec, H. Němec, P. Kužel, *Phys. Rev. B* **70**, 125205 (2004).

28. E. J. Yoffa, *Appl. Phys. Lett.* **36**, 37 (1980).

29. J. F. Young, H. M. van Driel, *Phys. Rev. B* **26**, 2147 (1982).

30. L. Huang, J. P. Callan, E. N. Glezer, E. Mazur, *Phys. Rev. Lett.* **80**, 185 (1998).

31. A. Dargys, J. Kundrotas, *Handbook on physical properties of Ge, Si, GaAs and InP* (Science and Encyclopedia Publishers, Vilnius, Lithuania, 1994).

32. D. E. Aspnnes, A. A. Studna, *Phys. Rev. B* **7**, 4605 (1973).

33. M. Alouani, L. Brey, N. E. Christensen, *Phys. Rev. B* **37**, 1167 (1988).

34. A. D. Yoffe, *Adv. Phys.* **42**, 173 (1993).

35. J. A. Kash, J. C. Tsang, in *Spectroscopy of nonequilibrium electrons and phonons,* C. V. Shank, B. P. Zakharchenya, Eds. (North-Holland, Amsterdam, 1992).

36. D. von der Linde, J. Kuhl, H. Klingenberg, *Phys. Rev. Lett.* **44**, 1505 (1980).

37. J. J. Baumberg, D. A. Williams, K. Köhler, *Phys. Rev. Lett.* **78**, 3358 (1997).

38. D. M. Pennington, C. B. Harris, *IEEE J. Quantum Electron.* **28**, 2523 (1992).

39. J. Shah, *Hot carriers in semiconductor nanostructures : Physics and applications* (Academic Press, Boston, 1992).

40. J. Shah *et al.*, *Phys. Rev. Lett.* **59**, 2222 (1987).

41. D. Y. Oberli, J. Shah, T. C. Damen, *Phys. Rev. B* **40**, 1323 (1989).

42. E. J. Yoffa, *Phys. Rev. B* **23**, 1909 (1981).

43. F. A. Lindemann, *Phys. Z.* **11**, 609 (1910).

44. J. F. Vetelino, S. P. Gaur, S. S. Mitra, *Phys. Rev. B* **5**, 2360 (1972).

45. P. Saeta, J. K. Wang, Y. Siegal, N. Bloembergen, E. Mazur, *Phys. Rev. Lett.* **67**, 1023 (1991).

46. N. Bloembergen, in *Laser ablation: Mechanisms and applications II,* J. C. Miller, D. B. Geohegan, Eds. (American Institute of Physics Conference Proceedings 288, Woodbury, New York, 1994), pp. 3-10.

47. A. Rousse, C. Rischel, J.-C. Gauthier, *Rev. Mod. Phys.* **73**, 17 (2001).

48. C. Bressler, M. Chergui, *Chem. Rev.* **104**, 1781 (2004).

49. A. M. Lindenberg *et al.*, *Science* **308**, 392 (2005).

50. M. Bargheer, N. Zhavoronkov, M. Woerner, T. Elsaesser, *Chemphyschem* **7**, 783 (2006).

51. B. J. Siwick, J. R. Dwyer, R. E. Jordan, R. J. D. Miller, *Chem. Phys.* **299**, 285 (2004).

52. S. H. Nie, X. Wang, H. Park, R. Clinite, J. M. Cao, *Phys. Rev. Lett.* **96**, 025901 (2006).

53. J. H. Bechtel, *J. Appl. Phys.* **46**, 1585 (1975).

54. H. E. Elsayed-Ali, P. M. Weber, in *Time-resolved diffraction,* J. R. Helliwell, P. M. Rentzepis, Eds. (Oxford Univ. Press, Oxford, 1997), pp. 284.

55. M. Harb *et al.*, *J. Phys. Chem. B* **110**, 25308 (2006).

56. C. Thomsen, H. T. Grahn, H. J. Maris, J. Tauc, *Phys. Rev. B* **34**, 4129 (1986).

57. J. M. Thomas, *Angew. Chem. Int. Ed.* **43**, 2606 (2004).

58. D. L. Dorset, *Z. Kristallogr.* **218**, 237 (2003).

59. D. L. Dorset, *Acta Cryst. B* **52**, 753 (1996).

60. T. E. Weirich, J. L. Lábár, X. Zou, Eds., *Electron crystallography : Novel approaches for structure determination of nanosized materials*, (Springer, Dordrecht, Netherlands, 2006).

61. E. Yablonovitch, T. J. Gmitter, R. Bhat, *Phys. Rev. Lett.* **61**, 2546 (1988).

62. U. Strauss, W. W. Ruhle, K. Kohler, *Appl. Phys. Lett.* **62**, 55 (1993).

63. J. Singh, *Electronic and optoelectronic properties of semiconductor structures* (Cambridge Univ. Press, Cambridge, 2003), pp. 241-243.